

Symbiosis of radio-emitting winds and a jet in a super-Eddington active galactic nucleus

Xiaolong Yang (✉ yangxl@shao.ac.cn)

Shanghai Astronomical Observatory, CAS

Ailing Wang

Shanghai Astronomical Observatory <https://orcid.org/0000-0002-7351-5801>

Su Yao

Max-Planck-Institute for Radio Astronomy <https://orcid.org/0000-0002-9728-1552>

Tao An

Shanghai Astronomical Observatory <https://orcid.org/0000-0003-4341-0029>

Jun Yang

Chalmers University of Technology <https://orcid.org/0000-0002-2322-5232>

Luis Ho

Peking University

Minfeng Gu

Shanghai Astronomical Observatory

Willem Baan

ASTRON Neth Inst for Radio Astronomy

Ran Wang

Kavli Institute

Xiang Liu

Xinjiang Astronomical Observatory, CAS

Xiaoyu Hong

Shanghai Astronomical Observatory, CAS

Xue-Bing Wu

Peking University

Yingkang Zhang

Shanghai Astronomical Observatory, Key Laboratory of Radio Astronomy, Chinese Academy of Sciences

<https://orcid.org/0000-0001-8256-8887>

Wei Zhao

Shanghai Astronomical Observatory, CAS

Keywords: black hole growl, radio-emitting winds, super-critical accretion

Posted Date: June 7th, 2021

DOI: <https://doi.org/10.21203/rs.3.rs-588601/v1>

License:  This work is licensed under a Creative Commons Attribution 4.0 International License.

[Read Full License](#)

Symbiosis of radio-emitting winds and a jet in a super-Eddington active galactic nucleus

Xiaolong Yang^{1,2,*}, Ailing Wang^{1,3}, Su Yao⁴, Tao An¹, Jun Yang⁵, Luis C. Ho^{2,6}, Minfeng Gu⁷, Willem A. Baan^{8,9}, Ran Wang², Xiang Liu⁸, Xiaoyu Hong¹, Xue-bing Wu^{2,6}, Yingkang Zhang¹, Wei Zhao¹

¹Shanghai Astronomical Observatory, Key Laboratory of Radio Astronomy, Chinese Academy of Sciences, Nandan Road 80, 200030, China

²Kavli Institute for Astronomy and Astrophysics, Peking University, Beijing 100871, China

³University of Chinese Academy of Sciences, 19A Yuquanlu, Beijing 100049, China

⁴Max-Planck-Institut für Radioastronomie, Auf dem Hügel 69, 53121 Bonn, Germany

⁵Department of Space, Earth and Environment, Chalmers University of Technology, Onsala Space Observatory, SE-439 92 Onsala, Sweden

⁶Department of Astronomy, School of Physics, Peking University, Beijing 100871, China

⁷Key Laboratory for Research in Galaxies and Cosmology, Shanghai Astronomical Observatory, Chinese Academy of Sciences, 200030 Shanghai, P.R. China

⁸Xinjiang Astronomical Observatory, Key Laboratory of Radio Astronomy, Chinese Academy of Sciences, 150 Science 1-Street, 830011 Urumqi, P.R. China

⁹Netherlands Institute for Radio Astronomy ASTRON, NL-7991 PD Dwingeloo, the Netherlands

Super-critical accretion is the most powerful episode in nursing the black hole growth ¹ and works in several types of objects ²⁻¹². Given that the inverse correlation between radio loudness and Eddington ratio ¹², the super-Eddington active galactic nuclei (AGNs) hold the extremely radio-quiet end of AGNs. Regarding the existence of jet in super-Eddington or radio-quiet AGNs, it's still unclear ^{13,14}. Years of studies indicate nearly all types of super-Eddington accreting systems can launch a jet ^{3,5-11,15,16}, with one exception: no clear evidence to show jet in super-Eddington AGNs. Observations and theoretical works suggest that super-Eddington accretion can drive high-speed wind-like outflows ^{17,18}, therefore produce radio emission through synchrotron (shocked winds) and bremsstrahlung mechanisms. However, such a radio-emitting wind has not been observed in super-Eddington systems except for the Galactic micro-quasar SS 433 ^{19,20}. In principle, high resolution very long baseline interferometry (VLBI) observation can directly map the inner structure of super-Eddington AGNs. Here, we report the discovery of the coupling of jet and radio-emitting winds in a nearby super-Eddington AGN, I Zw 1. Its parsec-scale jet exhibits a wiggling, we interpret this as a jet precession. All the features make I Zw 1 act as a scaled-up version of SS 433. The observations favour that jet can be launched in extremely radio-quiet AGNs and ubiquitous in super-Eddington accreting systems. The jet wiggling or precession can produce a large aperture-angle shock, which emphasises the jet's contribution to gas feedback. As the jet precession was also discovered in other super-Eddington systems such as SS 433 ³ and V404 Cygni ⁵, it is possible that there is a correlation with each other.

*Corresponding author

39 IZw 1 is one of the closest quasars at a redshift of $z = 0.0589$ ²¹, and is regarded as an
 40 archetypal narrow-line Seyfert 1 galaxy (NLS1) based on its optical properties^{22,23}. The black hole
 41 mass of IZw 1 was estimated by the reverberation mapping method to be $M_{\text{BH}} = 9.3 \times 10^6 M_{\odot}$
 42²⁴. The inferred bolometric luminosity of $L_{\text{bol}} = 10^{45.50} - 10^{45.68} \text{ erg s}^{-1}$ (refs.²⁵) exceeds its
 43 Eddington limit, indicating a super-Eddington accretion system with an Eddington ratio of $\lambda_{\text{Edd}} =$
 44 $2.77 - 4.20$ ¹. IZw 1 is a radio-quiet active galactic nucleus (AGN) with radio loudness $\mathcal{R} = 0.35$
 45 (refs.¹², fn.²). Radio emission from radio-quiet AGNs is complex and remains a subject of debate
 46¹³. On the other hand, the presence of jets in super-Eddington accretion systems, based on the
 47 inverse correlation between radio loudness and Eddington ratio¹² is also a question to be explored.
 48 IZw 1, as an extreme example of a nearby super-critical accretion and radio-quiet AGN, provides
 49 an ideal laboratory for studying the radio emission structure and its nuclear environment with high
 50 spatial resolutions.

51 We observed IZw 1 on 2018 September 23 with 10 telescopes of the Very Long Baseline
 52 Array (VLBA) at L-band (1.5 GHz) and on 2020 November 17 with 19 telescopes of the European
 53 VLBI Network (EVN) plus the enhanced Multi-Element Remote-Linked Interferometer Network
 54 (*e*-MERLIN) at C-band (5 GHz), obtaining angular resolutions of 5 and 1 mas at L-band and
 55 C-band, respectively. In addition, we also analysed the archived Very Large Array (VLA) and
 56 *e*-MERLIN data. The observations and data processing are referred to Methods. The upper panel
 57 of Figure 1 shows the L-band VLBA image, displaying a continuous emission structure elongated
 58 along the east-west direction with an extent of ~ 45 parsec (pc). The central component is the
 59 brightest and two weaker components located on opposite sides, reminiscent of a core and two-
 60 sided jet structure. The lower panel of Figure 1 shows a higher-resolution (~ 1 mas, or ~ 1.14 pc)
 61 image obtained from the C-band EVN plus *e*-MERLIN observations. The bright central component
 62 is resolved into a series of knots, all of which have brightness temperatures higher than 10^6 K at
 63 both 1.5 and 5 GHz (Table 1) and show steep spectra (Figure 2), ruling out models involving dense
 64 star-forming regions²⁶ and thermal free-free radiation from the hot molecular disk surrounding the
 65 nucleus²⁷. Furthermore, with the core identified in radio and optical (see below), the asymmetric
 66 radio structure suggests Doppler boosting effect for the approaching jet.

67 The nucleus of IZw 1 has an optical position (i.e. optical nucleus: R.A. = $00^{\text{h}}53^{\text{m}}34^{\text{s}}.933288 \pm$
 68 0.000187 , DEC. = $+12^{\circ}41'35''.93081 \pm 0.00017$, J2000)^{28,29}, closer to the component Wa (Figure
 69 1), which has the highest brightness temperature $\log T_{\text{B}} = 12.39$ K. An AGN core generally has
 70 a flat radio spectrum due to the optically-thick synchrotron emission ($\alpha > -0.5$ ³). In the full
 71 resolution image of C-band, the component Wa fits well with the optical nucleus position and has
 72 a flat radio spectrum (Figure 2, $\alpha \sim -0.4$). Therefore, component Wa is most likely to be the
 73 radio core. As we produced the ridgeline and radio spectral index map based on the full reso-
 74 lution L-band and tapered C-band images, only component W can be identified in the relatively
 75 low-resolution images. Therefore, in the discussion of jet structures, we alternatively selected the

¹ $\lambda_{\text{Edd}} \equiv L_{\text{bol}}/L_{\text{Edd}}$; L_{bol} is the bolometric luminosity, $L_{\text{Edd}} = 3.2 \times 10^4 (M_{\text{BH}}/M_{\odot})L_{\odot}$ is the Eddington
 luminosity, M_{BH} is the black hole mass.

² $\mathcal{R} = 1.3 \times 10^5 (L_5/L_B)$; L_5 is the radio luminosity at 5 GHz and L_B is the optical luminosity of the nucleus at
 $\lambda_B = 4400 \text{ \AA}$; Radio-quiet AGNs are defined as $\mathcal{R} < 10$.

³ $S_{\nu} \propto \nu^{\alpha}$; S_{ν} is the flux density and ν is the frequency

76 flattest radio spectral position (see Figure 2) along the ridgeline as the central reference point for
 77 the jet trajectory, which is consistent with component W within $1\text{-}\sigma$ uncertainty. The location is
 78 at $\Delta\text{R.A.} = 2.18$ (mas, J2000), $\Delta\text{DEC.} = -2.18$ (mas, J2000) with respect to the *Gaia* optical nu-
 79 cleus. Regarding the jet reference, the radio spectral index decreases rapidly in both extending
 80 directions (right panel of Figure 2), further confirming the core environment and the jet originated
 81 from there. The steepening of the spectra with increasing distance is due to the radiative losses of
 82 synchrotron-emitting plasma³⁰.

83 There is no theoretical consensus on whether there are jets in a super-Eddington system and
 84 how the jets are produced. The observed inverse correlation between the radio loudness and the
 85 Eddington ratio¹² suggests that the jet is progressively suppressed as the Eddington ratio increases,
 86 mainly due to the Papaloizou-Pringle instability³¹. As the accretion rate approaches about one-
 87 third of the Eddington limit, the Papaloizou-Pringle instability destroys the jet-producing region
 88 of the disc, suppressing the jet production. Relativistic winds arising from super-Eddington accre-
 89 tion disc are sometimes considered to be a secondary mechanism for further jet suppression^{32,33}.
 90 However, recent studies have shown that a relatively rapidly developing magnetic field may induce
 91 magneto-rotational instability^{34,35} that can stabilise the disc³⁶, thus giving a chance to form the
 92 jet. There is growing observational evidence for the existence of jets in super-critical accretion
 93 systems, such as accreting X-ray pulsars⁶, black hole X-ray binaries^{3,5,15,19}, and tidal disruption
 94 events⁷⁻¹¹.

95 In the 1.5 and 5 GHz images, we find an excess of transverse emission in the north-south
 96 direction (denoted as N and S at 1.5 and 5 GHz). The transverse emission at 5 GHz is further
 97 confirmed in the tapered image and well overlapped with the 1.5 GHz image (contours in the left
 98 panel of Figure 2). We find the transverse emission seems to arise from the bright jet components
 99 (W/Wa and E2), and their high brightness temperatures $> 10^6$ K make them unlikely to result
 100 from star-forming activities. These features resemble the radio structure in SS 433³⁷, in which the
 101 transverse emission has a steep radio spectrum $\alpha = -1$ ¹⁹, indicating that it originates from wind-
 102 like outflow (shocked winds) through the synchrotron process. The wind-like equatorial outflow
 103 in SS 433 maintains at a projected distance of ~ 20 mas^{20,37} from the core, corresponding to a size
 104 of $\sim 10^{8.5} R_g$, where R_g is the Schwarzschild radius³⁸. By comparison, the transverse emission in
 105 I Zw 1 also has a steep radio spectrum ($\alpha \sim -1$, Figure 2) and the base of the transverse emission
 106 maintains at a size of ~ 10 mas, corresponding to $\sim 10^{7.0} R_g$, which can be explained by a similar
 107 synchrotron process of the relativistic electrons accelerated by the wind-driven shocks³⁹.

108 The wind-like outflow in the super-Eddington regime has long been suggested by analytical
 109 and numerical models¹⁸. It is found that the wind-like outflow is ubiquitous in black hole X-ray
 110 binaries when it is in a high accretion state close to the Eddington limit¹⁷. There are also signs
 111 of wind-like radio-emitting outflows in high accreting AGNs⁴⁰. I Zw 1 do host strong multiscale
 112 outflows: an ultrafast wind-like outflow with a velocity of $> 0.25c$ obtained from the fitting of
 113 the iron K-line profile⁴¹, an ionised ultraviolet gas outflow with a velocity of 1870 km s^{-1} ⁴² and a
 114 neutral gas outflow with a velocity of 45 km s^{-1} ⁴³. Interestingly, the neutral gas outflow coincides
 115 with the direction of N and S components.

116 The radio emission from the wind-like outflow (shocked winds) in I Zw 1 may arise from the

117 jet collision with the massive outflow (perpendicular to an outer accretion disk) as was suggested
118 in SS 433⁴⁴ or a parsec-scale dense molecular gas disc/torus (jet-induced wind-like outflow, when
119 jet-ISM collision, the jet plasma tends to flow laterally along the decreasing gradient), or both. The
120 jet-ISM collision interpretation is supported by the parameter $\eta < 1$ (Figure 6), which suggests
121 that a dense environment hinders the expansion of the jet plasma⁴⁵. Further support is provided by
122 recent observations of IZw 1 at other bands: the direction of the kilo-parsec-scale molecular gas
123 disc was found^{46,47} to be approximately along the parsec-scale jet direction here, and a radius of
124 ~ 7 mas (~ 8 pc) torus is also proposed⁴⁸.

125 Furthermore, we know that jet direction is a good indicator of BH spin⁴⁹ or inner accre-
126 tion disk orientation⁵⁰, i.e. jet is either along the BH spin direction or inner accretion disk axis.
127 Our observations reveal that the jet direction in IZw 1 is along the kpc-scale molecular disk^{46,47},
128 which is suggesting that the kpc-scale molecular disk (direction of the axis) is tilted with the inner
129 accretion disk axis or BH spin.

130 **Methods**

131 **VLBI observations** We observed IZw 1 on 2018 September 23 with ten antennas (full array)
132 of the Very Long Baseline Array (VLBA) and on 2020 November 17 with nineteen antennas of
133 the European VLBI Network (EVN) plus the enhanced Multi-Element Remote-Linked Interfer-
134 ometer Network (*e*-MERLIN). The VLBA observations were carried out at L-band (1.5 GHz, the
135 project code BY145), and the EVN+*e*-MERLIN observations were conducted at C-band (5 GHz,
136 the project code EY037), respectively. The total VLBA observing time is 2 h with a data record-
137 ing rate of 2 Gbps, while the total time of the EVN+*e*-MERLIN observation is 8 h with a data
138 recording rate of 4 Gbps. Both observations were performed in the phase-referencing mode, using
139 J0056+1341 (R.A.: $00^{\text{h}}56^{\text{m}}14.8161^{\text{s}}$, Dec.: $+13^{\circ}41'15.755''$) as the phase reference calibrator.

140 **VLBI data reduction** We calibrated the VLBI data in the Astronomical Image Processing System
141 (AIPS), a software package developed by the National Radio Astronomy Observatory (NRAO) of
142 U.S.⁵¹, following the standard procedure. A-prior amplitude calibration was performed using the
143 system temperatures and the antenna gain curves provided by each station. The earth orientation
144 parameters were obtained and corrected using the measurements from the U.S. Naval Observatory
145 database and the ionospheric dispersive delays were corrected based on a map of the total electron
146 content provided by the GPS satellite observations⁴. The opacity and parallactic angles were also
147 corrected based on the auxiliary files attached to the data. The delay of the visibility phase and the
148 telescope bandpass were calibrated using the bright radio source 3C 454.3. Finally, we performed
149 a global fringe-fitting on the phase-referencing calibrator J0056+1341 by assuming a point source
150 model to solve miscellaneous phase delays.

151 The phase calibrator J0056+1341 shows a core and a jet extending ~ 100 mas to the north
152 (see the 1.5 and 5 GHz images in Figure 5). We first performed self-calibration to the calibrator
153 and obtained its CLEAN model, which was then used as the input model to re-solve the phases in
154 AIPS. This operation can eliminate the phase reference errors due to the jet structure. We applied

⁴<https://cddis.nasa.gov>

155 the solutions obtained from the calibrator by re-running fringe fitting to the target. Next, the data
156 from the target source is exported to DIFMAP⁵² for deconvolution. No self-calibration was used
157 for the target since it is too weak and resolved, with a signal-to-noise ratio of ~ 30 and ~ 14 at 1.5
158 and 5 GHz, respectively.

159 We performed CLEAN and model fitting algorithms to produce radio maps. The CLEAN
160 algorithm is suitable for compact and isolated emission structures, however, it has serious problems
161 in recovering a complex emission source when the uv sampling is poor, as is always common in
162 VLBI observations. In contrast, the model fitting procedure has the desirable property to take
163 into account the statistical details, and is suitable for reliable parametric representation of the
164 sparsely sampled visibility data. It is important to note that the solutions for model fitting are more
165 or less not unique when complex structures are to be handled. Here we use the delta function
166 rather than the usually used Gaussian function for model fitting, as the delta function has fewer
167 parameters than the Gaussian model and is sensitive to asymmetric emission regions. The resulting
168 images are shown in Figures 3 and 4. The CLEAN and model-fit images at both L- and C-band
169 are very consistent, although several components (X, E3a, and E3b) in the C-band image with
170 delta-function model fitting have a slightly different structure to that in the CLEAN image. The
171 difference is mainly in the weak and diffused structures due to the reason mentioned above, *i.e.*,
172 the poor uv-coverage particularly on the long baselines and the limited common observing time on
173 the east-west baselines. IZw 1 also shows residual emission in the north and south directions at
174 both 1.5 and 5 GHz, after removing the central bright components, strongly indicating that some
175 diffused emission cannot be recovered at the full resolution map. Therefore, we also produced
176 a uv-tapered map to reduce the weight of the long-baseline visibilities (and thus also reduce the
177 resolution) in an attempt to recover the weak and extended emission.

178 **Archived MERLIN data** Two MERLIN C-band (4.99 GHz) datasets of the target IZw 1 are avail-
179 able in the MERLIN data archive⁵. These data were observed on 1996 December 1 with six an-
180 tennas: Defford (De), Cambridge (Ca), Knockin (Kn), Darnhall (Da), Mark II (Mk), and Tabley
181 (Ta), and 1997 November 6 with five antennas (De, Ca, Kn, Da, Ta). The two MERLIN observa-
182 tions provide a minimum baseline of 0.07 M λ (~ 4 km) and 0.47 M λ (~ 28 km), respectively, and a
183 maximum baseline of 3.62 M λ (~ 217 km) for both with a resolution of ~ 0.1 arcsec. The calibra-
184 tor J0106+1300 (RA: 01^h06^m33.3558^s, Dec: +13^o00'02.608'') was used for phase reference, and
185 3C 286 and OQ 208 were used as the primary flux density scale and bandpass calibrator for both
186 datasets. The phase of the archived MERLIN data has already been calibrated in AIPS, including
187 preliminary bandpass and flux density scale calibration, phase and amplitude calibrations. We im-
188 ported the calibrated data into DIFMAP for manual imaging and self-calibration. In both datasets,
189 the target is detected with a signal-to-noise ratio above 7, self-calibration has not been used. A
190 two-dimensional Gaussian model was fitted to the visibility data to obtain the integrated and peak
191 flux density, which are shown in Table 2.

192 **Archived VLA data** We retrieved the raw visibility data of IZw 1 observed by the Very Large
193 Array (VLA) from the NRAO data archive⁶, including historical VLA and the newly observed Karl

⁵<http://www.merlin.ac.uk/archive/>

⁶<https://archive.nrao.edu/archive/advquery.jsp>

194 G. Jansky VLA (JVLA) data. Although some data have been published (see Table 2), to ensure
195 consistency in the data reduction, we performed a manual calibration for all available datasets using
196 the Common Astronomy Software Application (CASA v5.1.1) ⁵³. Our data reduction followed the
197 standard routines described in the CASA cookbook. We adopted the ‘Perley-Butler 2017’ flux
198 density standard ⁵⁴ to set the overall flux density scale for the primary flux calibrator, and then
199 bootstrapped the secondary flux density calibrators and the target. For the historical VLA datasets,
200 we determined the gain solutions using a nearby phase calibrator and transferred them to the target
201 IZw 1. For the JVLA datasets, we also determined antenna delay and bandpass by fringe-fitting
202 the visibilities. For the data observed after 1998, we performed an ionosphere correction using the
203 data obtained from the CDDIS archive. Deconvolution, self-calibration, and model-fitting were
204 performed in DIFMAP. The final images were created using natural weighting. Due to the good
205 uv-coverage of the VLA, simple emission structure, and high signal-to-noise ratio (SNR>9), the
206 VLA data allow for self-calibration using a well-established model. For data with lower SNR, we
207 used three times the image noise as the upper limit for the flux density.

208 **Astrometry of the VLBI data** The position uncertainty of the CLEAN components was esti-
209 mated as $\sim 20\%$ of the restoring beam dimensions in the naturally-weighted image. For isolated
210 components, we estimate the uncertainties as $\text{FWHM}/(2 \times \text{SNR})$, where FWHM is the full width
211 at half maximum of Gaussian components or the restoring beam for Delta components, and SNR
212 is the ratio of emission peak to the noise. The position errors of the phase-referencing calibrator
213 are $0.34 \mu\text{as}$ and $0.07 \mu\text{as}$ in 1.5 and 5 GHz images, respectively.

214 In phase-referencing observations, the coordinates of the target are referenced to the close
215 calibrator, however, during the self-calibration process, the absolute coordinate position of the
216 phase-referencing calibrator is lost and the brightest feature of the image is shifted to the phase
217 centre of the map. In general, due to the frequency-dependent shift of the optically thick compo-
218 nent’s peak and the slightly different distribution of the radio emission at different resolutions, the
219 brightest component may not be at the same position from one observation to another. This would
220 induce an offset between two images, in the form of astrometric error. The alignment between the
221 images of the two observations can be done using an optically thin component, whose position is
222 less affected by the frequency-dependent opacity effect, as a reference.

223 For VLBI observations in both L and C bands, we used J0056+1341 as the phase-referencing
224 calibrator, which has a flat-spectrum radio core. The absolute astrometric position of J0056+1341
225 is derived from the VLBA X-band (7.6 GHz) observations. Since neither the C- and X-band data
226 from Astrogeo ⁷ are self-calibrated, the core-shift at C-band can be directly estimated as $\Delta\text{R.A.}$
227 $\sim 0.70 \text{ mas}$, $\Delta\text{DEC.} \sim -0.20 \text{ mas}$ with respect to the 7.6 GHz data, the most accurate absolute
228 astrometric position of J0056+1341 at C-band can be determined accordingly. J0056+1341 also
229 has a significant offset between C and L bands (see Figure 5) in our observations, and the offset
230 of the VLBA L-band image is determined using the optically thin component of the jet, estimated
231 as $\Delta\text{R.A.} = 1.742 \pm 0.035 \text{ mas}$, $\Delta\text{DEC.} = -3.228 \pm 0.035 \text{ mas}$ to the EVN+e-MERLIN C-band
232 image.

⁷<http://astrogeo.org/>

233 For target IZw 1, we use the position of the brightest component (optically thin) in the ta-
 234 pered EVN+*e*-MERLIN C-band image (the upper panel in Figure 4) to match the VLBA L-band
 235 image which has a similar beam size. The peak position of the L-band image was moved to
 236 match the C-band image by $\Delta\text{R.A.} = 1.3308 \pm 0.035$ mas, $\Delta\text{DEC.} = -0.77024 \pm 0.035$ mas.
 237 The optical emission centroid of the second data release ⁸ of the *Gaia* mission ^{28,29} is R.A.=
 238 $00^{\text{h}}53^{\text{m}}34^{\text{s}}.933288 \pm 0.000012$, DEC.= $+12^{\circ}41'35''.93081 \pm 0.00017$ (J2000), including astro-
 239 metric excess noise error of 0.14 mas. The optical core IZw 1 located in the radio emission region.

240 The *Gaia* position indicates the compact and brightest feature in the optical band, which
 241 we use as the optical nucleus. In radio bands, we identify the radio core based on the compact
 242 component with a flat spectrum, furthermore, an AGN core is defined as the origin of a jet which
 243 should naturally locate on the jet trajectory. In the L-band image, the component W is closer to
 244 the optical nucleus and has the flat radio spectrum, the radio brightness temperature is $\log T_B =$
 245 10.57 K. In the C-band image, the component Wa has the highest brightness temperature ($\log T_B =$
 246 12.39 K) and is closest to the optical nucleus, which is most possible as the radio core. However,
 247 the component Wa is slightly offset from the jet trajectory (Figure 7), which makes it complex to be
 248 used as the reference point for the jet trajectory. As we produce ridgeline and radio spectral index
 249 map (Figure 2) based on the tapered (with reduced resolution) C-band and L-band images, only
 250 the component W can be identified there. On the discussion of jet structures, we have alternatively
 251 selected a reference point that located at the jet ridgeline and shows the flattest radio spectrum (the
 252 curve peak in the right panel of Figure 2), with no surprise that the position is consistent with the
 253 component W within $1\text{-}\sigma$ position errors (see Figure 7).

254 **Radio Spectrum** To obtain the radio spectral index, we first checked the variability of IZw 1.
 255 Figure 9 shows the radio flux density versus the observing epoch, and the largest variability we
 256 can identify is $\sim 8\%$, which is from the VLA A-array observations at C-band between the epoch
 257 1983 and 1995. Since there is no significant variability on a time scale of ~ 30 years, we plot the
 258 radio flux density versus the frequency in Figure 10. The least-square fitting gives an overall radio
 259 spectral index of -0.88 ± 0.10 . From Figure 10, we found the radio flux density changes with the
 260 size of the synthesis beam. The radio spectral index between 1.4 and 5 GHz by using the datasets
 261 with a similar resolution, *i.e.*, $1.3 \sim 1.5$ and $4.3 \sim 5.3$ arcsec, is -0.69 ± 0.13 and -0.60 ± 0.03 ,
 262 slightly flatter than the overall value.

263 For the high-resolution data observed with the VLBA and EVN+*e*-MERLIN, in order to
 264 obtain its spectral index distribution, we obtained a spectral index map following the procedure
 265 described in ³⁰. Here we used the uv-tapered image by 0.5 at $20 \text{ M}\lambda$ at 5 GHz and restored it to
 266 match the 1.5 GHz map. The spectral index was calculated pixel by pixel between the 1.5 and
 267 5 GHz total intensity maps. For a given frequency, pixels with an intensity less than $3\sigma_{rms}$ were
 268 removed. The spectral index map between 1.5 and 5 GHz is shown in the left panel of Figure 2.

269 **Radio flux density and Brightness Temperature** We estimated the uncertainties of integrated
 270 flux density S_i and peak flux density S_p using the expression $\sigma_i = \sqrt{2.5\sigma_{rms}^2 + (0.01S_i)^2}$ ⁵⁵ and
 271 $\sigma_p = \sqrt{\sigma_{rms}^2 + (1.5\sigma_{rms})^2} \approx 1.8\sigma_{rms}$ ⁵⁶, respectively, where σ_{rms} is the RMS noise estimated in

⁸<https://gea.esac.esa.int/archive/>

272 a blank sky zone far away from the target source. The radio brightness temperature was estimated
 273 by using the formula ⁵⁷:

$$T_B = 1.8 \times 10^9 (1 + z) \frac{S_i}{\nu^2 \phi_{min} \phi_{maj}} \text{ (K)}, \quad (1)$$

274 where S_i is the integrated flux density of each Gaussian model component in units of mJy (column
 275 5 of Table 1); ϕ_{min} and ϕ_{maj} are the minor and major axes lengths of the full width at half maximum
 276 (FWHM) of the Gaussian model or the restored beam in milli-arcsec; ν is the observing frequency
 277 in GHz (column 2 of Table 1), and z is the redshift. To estimate the component size, we fit a
 278 Gaussian model to the 1.5 and 5 GHz data by using natural weights, the fitting only fills several well
 279 symmetric and isolated components (see column 6 of Table 1). Note that the Gaussian model is not
 280 a good representation of the emission distribution when the complex radio structure is encountered
 281 in a poor uv-coverage, for those components without a Gaussian model representation, we use
 282 the synthesised beam instead as the component size. The estimated 1.5 GHz and 5 GHz radio
 283 brightness temperatures are listed in Column 7 of Table 1. Since the measured component size
 284 is only the upper limit, the radio brightness temperature should be considered as the lower limit.
 285 We also estimated a total radio flux density using the tapered images at 1.5 and 5 GHz, which
 286 is 2.636 ± 0.098 and 0.614 ± 0.047 mJy, respectively, the corresponding angular size is ~ 50 and
 287 ~ 40 mas, respectively.

288 **Model-fitting of the helical jet structures** To obtain the trajectory of the main jet structures, we
 289 cleaned the C-band data by using a natural weight and a Gaussian tapering of 0.5 at uv radius
 290 $10 M\lambda$, the clean procedures stopped when the peak flux density in the dirty map dropped below
 291 $7\sigma = 5.75 \times 10^{-5}$ Jy/beam. The clean components appropriately show the linear jet trajectory,
 292 and here we designated the spectral peak along the jet line as the emitting origin and the reference,
 293 which is located at R.A.= 2.18 (mas), DEC.= -2.18 (mas) with respect to the *Gaia* position.

294 The total synchrotron emission from a single optically thin jet knot where the synchrotron-
 295 emitting plasma undergoes adiabatic expansion can be scaled ⁴⁵ as

$$J(\nu) \propto \nu^{\frac{1-p}{2}} R^{\frac{1-3p}{2}}, \quad (2)$$

296 where $p = 1 - \alpha$ and α is the spectral index of the emission ($S_\nu \propto \nu^\alpha$, ν is the frequency, R is
 297 the radius of a jet knot, assuming symmetric expansion of the approaching and receding jets. By
 298 taking the expansion of the plasma to be the form

$$R \propto t^\eta = \left(\frac{Dr}{v_i}\right)^\eta, \quad (3)$$

299 where r is the angular distance to the core and v_i is velocity on the sky plane, D is the distance from
 300 the observer to the target, η indicates the linearity of jet expansion ($R \propto t^\eta$), for linear expansion
 301 $\eta = 1$ and for the deceleration of the expanding plasma, $\eta < 1$. We can get

$$J(\nu) \propto \nu^{\frac{1-p}{2}} v_i^{-\eta \frac{1-3p}{2}} r^{\eta \frac{1-3p}{2}}, \quad (4)$$

302 Then the ratio of radio flux densities as seen by the observer is

$$\frac{S_{app}}{S_{rec}} = \left(\frac{1 + \beta \cos i}{1 - \beta \cos i} \right)^{k+\alpha} \left(\frac{L_{app}(t_{app})}{L_{rec}(t_{rec})} \right), \quad (5)$$

303 where S_{app} and S_{rec} are the flux density for approaching and receding jet components, respectively,
 304 $\beta = v/c$ is the jet speed in unit of speed of light c . t_{app} and t_{rec} are the times at which light leaves
 305 the approaching and receding knots, respectively, and L_{app} and L_{rec} is their luminosities, k takes
 306 value 2 in our case for a continuous jet. Here we know the velocities on the sky plane (or proper
 307 motions) at approaching v_{app} and receding v_{rec} jet knots have the relation

$$\frac{v_{app}}{v_{rec}} = \frac{1 + \beta \cos i}{1 - \beta \cos i}, \quad (6)$$

308 then

$$\frac{S_{app}}{S_{rec}} = \left(\frac{r(t_{app})}{r(t_{rec})} \right)^{\eta \frac{1-3p}{2}} \left(\frac{1 + \beta \cos i}{1 - \beta \cos i} \right)^{-\eta \frac{1-3p}{2} + k + \frac{p-1}{2}}, \quad (7)$$

309 where S_{app} and S_{rec} are the flux densities of a corresponding pair of approaching and receding
 310 knots, $r(t_{app})$ and $r(t_{rec})$ are their proper motion distances to the core. Here we fit our data with
 311 the model above, η as a free parameter, and introduce a new free parameter f_0 as the flux density
 312 scale, i.e.

$$f_0 = \frac{f_{0,app}}{f_{0,rec}} = \frac{1 + \beta \cos i}{1 - \beta \cos i}, \quad (8)$$

313 where $f_{0,app}$ and $f_{0,rec}$ are the flux density at the same distance in approaching and receding jet,
 314 respectively. At the same jet direction we have

$$S \propto r^{\eta \frac{1-3p}{2}} f_0^{-\eta \frac{1-3p}{2} + k + \frac{p-1}{2}}, \quad (9)$$

315 The flux density scale f_0 of approaching and receding jet and the jet expansion parameter η can
 316 be constrained based on the variation of the jet flux density with the distance from the core. In
 317 Figure 6, we show the constraints on parameters, and we take one percent of the integrated flux
 318 density as the error. Due to the limited data points and the effect of jet helical motion and colliding
 319 with dense medium, for example, the radio flux density at radius ~ 1 and ~ 10 mas (which does
 320 not take to constrain the parameters). In order to give a reasonable estimate of parameter f_0 and
 321 η , we select bright components for fitting, which are marked with blue (approaching jet) and red
 322 (receding jet) in Figure 6), we firstly fit the data points at the approaching jet with least-square,
 323 which yield $f_{0,app} = 3.10 \pm 0.07$ and $\eta = 0.22 \pm 0.02$, then fit the data points at receding jet
 324 with η fixed at 0.22, i.e. assuming the same environment for both approaching and receding jets,
 325 which yields the parameter $f_{0,rec} = 2.80 \pm 0.05$, with the formula 8, we can get the parameter
 326 $\beta \cos i = 0.050 \pm 0.002$.

327 We used a relativistic jet precession model ⁵⁸, where the jet projected on the plane of the sky
 328 can be determined by the following parameters: jet velocity $\beta = v/c$ where v is the jet speed;
 329 i is the jet inclination angle to the line of sight; the opening angle of the precessing jet cone ψ ;

330 the jet position angle to the north on the plane of the sky anti-clockwisely χ ; angular velocity of
 331 jet precession Ω ($\Omega = 2\pi/P$, where P is precession period); initial angle of jet precession or
 332 the precession angle of terminal jet components to the line of sight θ , positive value for an anti-
 333 clockwise rotating and vice versa. In this model, β and Ω are tightly correlated with i and only
 334 the i can be fitted separately, so we taking the relation $\beta \cos \theta = 0.050 \pm 0.002$ for an overall
 335 helical jet model-fitting. The parameters were determined by performing a Markov Chain Monte
 336 Carlo (MCMC) algorithm implemented with the ‘emcee’ package ⁵⁹, the off-axis features of the
 337 jet have been removed from the fitting and we only use the approaching jet (eastern part) for the
 338 model-fitting.

339 The posterior probability of the MCMC approach is shown in Figure 8, where each parame-
 340 ter is well determined. The best-fit values are those with the maximum posterior probability (50%
 341 quantiles of marginalised posteriors). Not surprisingly, the parameter i and Ω are tightly corre-
 342 lated, however with the good probability distribution of the parameter i , both parameters i and
 343 Ω are well determined simultaneously. The fit yields $i = 1.52^{+0.01}_{-0.02}$ (rad), $\psi = 0.10^{+0.02}_{-0.02}$ (rad),
 344 $\chi = 1.77^{+0.01}_{-0.01}$ (rad), $\theta = -2.38^{+1.06}_{-1.06}$ (rad) and $\Omega = 0.15^{+0.09}_{-0.06}$ (rad/yr) corresponding to $P =$
 345 41^{+27}_{-15} (yr). With the relation $\beta \cos i = 0.050 \pm 0.002$ and the estimated parameter i , the jet veloc-
 346 ity can be determined as $v = 0.70 - 1$ (c). In Figure 7, we show the jet trajectory presented by the
 347 parameters above.

- 348 1. Volonteri, M. & Rees, M. J. Rapid Growth of High-Redshift Black Holes. *ApJ* **633**, 624–629
 349 (2005).
- 350 2. Kaaret, P., Feng, H. & Roberts, T. P. Ultraluminous X-Ray Sources. *ARA&A* **55**, 303–341
 351 (2017).
- 352 3. Fabrika, S. The jets and supercritical accretion disk in SS433. *Astrophys. Space Phys. Res.*
 353 **12**, 1–152 (2004).
- 354 4. Done, C., Wardziński, G. & Gierliński, M. GRS 1915+105: the brightest Galactic black hole.
 355 *MNRAS* **349**, 393–403 (2004).
- 356 5. Miller-Jones, J. C. A. *et al.* A rapidly changing jet orientation in the stellar-mass black-hole
 357 system V404 Cygni. *Nature* **569**, 374–377 (2019).
- 358 6. van den Eijnden, J. *et al.* An evolving jet from a strongly magnetized accreting X-ray pulsar.
 359 *Nature* **562**, 233–235 (2018).
- 360 7. Bloom, J. S. *et al.* A Possible Relativistic Jetted Outburst from a Massive Black Hole Fed by
 361 a Tidally Disrupted Star. *Science* **333**, 203 (2011).
- 362 8. Burrows, D. N. *et al.* Relativistic jet activity from the tidal disruption of a star by a massive
 363 black hole. *Nature* **476**, 421–424 (2011).
- 364 9. Levan, A. J. *et al.* An Extremely Luminous Panchromatic Outburst from the Nucleus of a
 365 Distant Galaxy. *Science* **333**, 199 (2011).
- 366
- 367
- 368

- 369 10. Zauderer, B. A. *et al.* Birth of a relativistic outflow in the unusual γ -ray transient Swift
370 J164449.3+573451. *Nature* **476**, 425–428 (2011).
- 371 11. Mattila, S. *et al.* A dust-enshrouded tidal disruption event with a resolved radio jet in a galaxy
372 merger. *Science* **361**, 482–485 (2018).
- 373 12. Yang, X. *et al.* Radio Activity of Supermassive Black Holes with Extremely High Accretion
374 Rates. *ApJ* **904**, 200 (2020).
- 375 13. Panessa, F. *et al.* The origin of radio emission from radio-quiet active galactic nuclei. *Nature*
376 *Astronomy* **3**, 387–396 (2019).
- 377 14. Blandford, R., Meier, D. & Readhead, A. Relativistic Jets from Active Galactic Nuclei.
378 *ARA&A* **57**, 467–509 (2019).
- 379 15. Hjellming, R. M. & Johnston, K. J. Structure, strength and polarization changes in radio
380 source SS 433. *Nature* **290**, 100–107 (1981).
- 381 16. Mirabel, I. F. & Rodríguez, L. F. A superluminal source in the Galaxy. *Nature* **371**, 46–48
382 (1994).
- 383 17. Ponti, G. *et al.* Ubiquitous equatorial accretion disc winds in black hole soft states. *MNRAS*
384 **422**, L11–L15 (2012).
- 385 18. Takeo, E., Inayoshi, K. & Mineshige, S. Hyper-Eddington accretion flows on to black holes
386 accompanied by powerful outflows. *MNRAS* **497**, 302–317 (2020).
- 387 19. Paragi, Z. *et al.* The inner radio jet region and the complex environment of SS433. *A&A* **348**,
388 910–916 (1999).
- 389 20. Blundell, K. M., Mioduszewski, A. J., Muxlow, T. W. B., Podsiadlowski, P. & Rupen, M. P.
390 Images of an Equatorial Outflow in SS 433. *ApJ* **562**, L79–L82 (2001).
- 391 21. Ho, L. C. & Kim, M. Magellan Spectroscopy of Low-Redshift Active Galactic Nuclei. *ApJS*
392 **184**, 398–415 (2009).
- 393 22. Schmidt, M. & Green, R. F. Quasar evolution derived from the Palomar bright quasar survey
394 and other complete quasar surveys. *ApJ* **269**, 352–374 (1983).
- 395 23. Pogge, R. W. Narrow-line Seyfert 1s: 15 years later. *New A Rev.* **44**, 381–385 (2000).
- 396 24. Huang, Y.-K. *et al.* Reverberation Mapping of the Narrow-line Seyfert 1 Galaxy I Zwicky 1:
397 Black Hole Mass. *ApJ* **876**, 102 (2019).
- 398 25. Martínez-Paredes, M. *et al.* The dusty tori of nearby QSOs as constrained by high-resolution
399 mid-IR observations. *MNRAS* **468**, 2–46 (2017).

- 400 26. Condon, J. J., Huang, Z. P., Yin, Q. F. & Thuan, T. X. Compact Starbursts in Ultraluminous
401 Infrared Galaxies. *ApJ* **378**, 65 (1991).
- 402 27. Gallimore, J. F., Baum, S. A. & O’Dea, C. P. A direct image of the obscuring disk surrounding
403 an active galactic nucleus. *Nature* **388**, 852–854 (1997).
- 404 28. Gaia Collaboration *et al.* Gaia Data Release 2. Mapping the Milky Way disc kinematics. *A&A*
405 **616**, A11 (2018).
- 406 29. Gaia Collaboration *et al.* Gaia Data Release 2. Summary of the contents and survey properties.
407 *A&A* **616**, A1 (2018).
- 408 30. Hovatta, T. *et al.* MOJAVE: Monitoring of Jets in Active Galactic Nuclei with VLBA Experi-
409 ments. XI. Spectral Distributions. *AJ* **147**, 143 (2014).
- 410 31. Papaloizou, J. C. B. & Pringle, J. E. The dynamical stability of differentially rotating discs
411 with constant specific angular momentum. *MNRAS* **208**, 721–750 (1984).
- 412 32. Meier, D. On the Anticorrelation between High Accretion Luminosity and Radio Jet Ejection
413 in GRO J1655-40 and Other Objects. *ApJ* **459**, 185 (1996).
- 414 33. Nielsen, J. & Lee, J. C. Accretion disk winds as the jet suppression mechanism in the micro-
415 quasar GRS 1915+105. *Nature* **458**, 481–484 (2009).
- 416 34. Balbus, S. A. & Hawley, J. F. A Powerful Local Shear Instability in Weakly Magnetized Disks.
417 I. Linear Analysis. *ApJ* **376**, 214 (1991).
- 418 35. Hawley, J. F., Gammie, C. F. & Balbus, S. A. Local Three-dimensional Magnetohydrodynamic
419 Simulations of Accretion Disks. *ApJ* **440**, 742 (1995).
- 420 36. Bugli, M. *et al.* Papaloizou-Pringle instability suppression by the magnetorotational instability
421 in relativistic accretion discs. *MNRAS* **475**, 108–120 (2018).
- 422 37. Jeffrey, R. M., Blundell, K. M., Trushkin, S. A. & Mioduszewski, A. J. Fast launch speeds in
423 radio flares, from a new determination of the intrinsic motions of SS 433’s jet bolides. *MNRAS*
424 **461**, 312–320 (2016).
- 425 38. Bowler, M. G. SS 433: Two robust determinations fix the mass ratio. *A&A* **619**, L4 (2018).
- 426 39. Faucher-Giguère, C.-A. & Quataert, E. The physics of galactic winds driven by active galactic
427 nuclei. *MNRAS* **425**, 605–622 (2012).
- 428 40. Yang, J. *et al.* A radio structure resolved at the deca-parsec scale in the radio-quiet quasar PDS
429 456 with an extremely powerful X-ray outflow. *MNRAS* **482**, 1701–1705 (2019).
- 430 41. Reeves, J. N. & Braitto, V. A Momentum-conserving Accretion Disk Wind in the Narrow-line
431 Seyfert 1 I Zwicky 1. *ApJ* **884**, 80 (2019).

- 432 42. Laor, A., Jannuzi, B. T., Green, R. F. & Boroson, T. A. The Ultraviolet Properties of the
433 Narrow-Line Quasar I Zw 1. *ApJ* **489**, 656–671 (1997).
- 434 43. Rupke, D. S. N., Gültekin, K. & Veilleux, S. Quasar-mode Feedback in Nearby Type 1
435 Quasars: Ubiquitous Kiloparsec-scale Outflows and Correlations with Black Hole Properties.
436 *ApJ* **850**, 40 (2017).
- 437 44. Begelman, M. C., King, A. R. & Pringle, J. E. The nature of SS433 and the ultraluminous
438 X-ray sources. *MNRAS* **370**, 399–404 (2006).
- 439 45. Miller-Jones, J. C. A., Blundell, K. M. & Duffy, P. Jet Evolution, Flux Ratios, and Light-Travel
440 Time Effects. *ApJ* **603**, L21–L24 (2004).
- 441 46. Tan, Q.-H. *et al.* Resolving the Interstellar Medium in Ultraluminous Infrared QSO Hosts with
442 ALMA. *ApJ* **887**, 24 (2019).
- 443 47. Shangguan, J., Ho, L. C., Bauer, F. E., Wang, R. & Treister, E. AGN Feedback and Star
444 Formation of Quasar Host Galaxies: Insights from the Molecular Gas. *ApJ* **899**, 112 (2020).
- 445 48. Pasetto, A. *et al.* AGN Torus Detectability at Submillimeter Wavelengths: What to Expect
446 from ALMA Continuum Data. *ApJ* **872**, 69 (2019).
- 447 49. Blandford, R. D. & Znajek, R. L. Electromagnetic extraction of energy from Kerr black holes.
448 *MNRAS* **179**, 433–456 (1977).
- 449 50. Blandford, R. D. & Payne, D. G. Hydromagnetic flows from accretion disks and the production
450 of radio jets. *MNRAS* **199**, 883–903 (1982).
- 451 51. Greisen, E. W. *AIPS, the VLA, and the VLBA*, vol. 285 of *Astrophysics and Space Science*
452 *Library*, 109 (2003).
- 453 52. Shepherd, M. C. Difmap: an Interactive Program for Synthesis Imaging. In Hunt, G. & Payne,
454 H. (eds.) *Astronomical Data Analysis Software and Systems VI*, vol. 125 of *Astronomical So-*
455 *ciety of the Pacific Conference Series*, 77 (1997).
- 456 53. McMullin, J. P., Waters, B., Schiebel, D., Young, W. & Golap, K. CASA Architecture and
457 Applications. In Shaw, R. A., Hill, F. & Bell, D. J. (eds.) *Astronomical Data Analysis Soft-*
458 *ware and Systems XVI*, vol. 376 of *Astronomical Society of the Pacific Conference Series*, 127
459 (2007).
- 460 54. Perley, R. A. & Butler, B. J. An Accurate Flux Density Scale from 50 MHz to 50 GHz. *ApJS*
461 **230**, 7 (2017).
- 462 55. Hopkins, A. M. *et al.* The Phoenix Deep Survey: The 1.4 GHz Microjansky Catalog. *AJ* **125**,
463 465–477 (2003).
- 464 56. Hovatta, T. *et al.* MOJAVE: Monitoring of Jets in Active Galactic Nuclei with VLBA Experi-
465 ments. VIII. Faraday Rotation in Parsec-scale AGN Jets. *AJ* **144**, 105 (2012).

- 466 57. Ulvestad, J. S., Antonucci, R. R. J. & Barvainis, R. VLBA Imaging of Central Engines in
467 Radio-Quiet Quasars. *ApJ* **621**, 123–129 (2005).
- 468 58. Hjellming, R. M. & Johnston, K. J. An analysis of the proper motions of SS 433 radio jets.
469 *ApJ* **246**, L141–L145 (1981).
- 470 59. Foreman-Mackey, D., Hogg, D. W., Lang, D. & Goodman, J. emcee: The MCMC Hammer.
471 *PASP* **125**, 306 (2013).
- 472 60. Lense, J. & Thirring, H. Über den Einfluß der Eigenrotation der Zentralkörper auf die Be-
473 wegung der Planeten und Monde nach der Einsteinschen Gravitationstheorie. *Physikalische*
474 *Zeitschrift* **19**, 156 (1918).
- 475 61. Bardeen, J. M. & Petterson, J. A. The Lense-Thirring Effect and Accretion Disks around Kerr
476 Black Holes. *ApJ* **195**, L65 (1975).
- 477 62. Papaloizou, J. C. B. & Terquem, C. On the dynamics of tilted discs around young stars.
478 *MNRAS* **274**, 987–1001 (1995).
- 479 63. Begelman, M. C., Blandford, R. D. & Rees, M. J. Massive black hole binaries in active galactic
480 nuclei. *Nature* **287**, 307–309 (1980).
- 481 64. Schandl, S. & Meyer, F. Hercules X-1: coronal winds producing the tilted shape of the accre-
482 tion disk. *A&A* **289**, 149–161 (1994).
- 483 65. Lai, D. Warping of Accretion Disks with Magnetically Driven Outflows: A Possible Origin
484 for Jet Precession. *ApJ* **591**, L119–L122 (2003).
- 485 66. Pringle, J. E. Self-induced warping of accretion discs. *MNRAS* **281**, 357–361 (1996).
- 486 67. Liu, Z., Yuan, W., Lu, Y. & Zhou, X. Relativistic Fe $K\alpha$ line revealed in the composite X-
487 ray spectrum of narrow-line Seyfert 1 galaxies - do their black holes have averagely low or
488 intermediate spins? *MNRAS* **447**, 517–529 (2015).
- 489 68. Morganti, R. Archaeology of active galaxies across the electromagnetic spectrum. *Nature*
490 *Astronomy* **1**, 596–605 (2017).
- 491 69. Molina, J. *et al.* Compact Molecular Gas Distribution in Quasar Host Galaxies. *ApJ* **908**, 231
492 (2021).
- 493 70. Fenech, D. M., Muxlow, T. W. B., Beswick, R. J., Pedlar, A. & Argo, M. K. Deep MERLIN
494 5GHz radio imaging of supernova remnants in the M82 starburst. *MNRAS* **391**, 1384–1402
495 (2008).
- 496 71. Edelson, R. A. Broad-Band Properties of the CfA Seyfert Galaxies. I. Radio Properties. *ApJ*
497 **313**, 651 (1987).
- 498 72. Condon, J. J. *et al.* The NRAO VLA Sky Survey. *AJ* **115**, 1693–1716 (1998).

- 499 73. Barvainis, R. & Antonucci, R. Millimeter, Centimeter, and Carbon Monoxide Observations
500 of Radio-quiet Quasars and Luminous Seyfert 1 Galaxies Detected by IRAS. *ApJS* **70**, 257
501 (1989).
- 502 74. Barvainis, R., Lonsdale, C. & Antonucci, R. Radio Spectra of Radio Quiet Quasars. *AJ* **111**,
503 1431 (1996).
- 504 75. White, R. L., Becker, R. H., Helfand, D. J. & Gregg, M. D. A Catalog of 1.4 GHz Radio
505 Sources from the FIRST Survey. *ApJ* **475**, 479–493 (1997).
- 506 76. Dressel, L. L. & Condon, J. J. The Arecibo 2380 MHz survey of bright galaxies. *ApJS* **36**,
507 53–75 (1978).
- 508 77. Lacy, M. *et al.* The Karl G. Jansky Very Large Array Sky Survey (VLASS). Science Case and
509 Survey Design. *PASP* **132**, 035001 (2020).
- 510 78. Kellermann, K. I., Sramek, R., Schmidt, M., Shaffer, D. B. & Green, R. VLA Observations of
511 Objects in the Palomar Bright Quasar Survey. *AJ* **98**, 1195 (1989).

512 **Acknowledgements** This work is supported by the National Science Foundation of China (11721303,
513 11991052), the National Key R&D Programme of China (2016YFA0400702, 2018YFA0404602, 2018YFA
514 0404603), and Shanghai Sailing Program (21YF1455300). SY is supported by an Alexander von Hum-
515 boldt Foundation Fellowship. MFG is supported by the National Science Foundation of China (grant
516 11873073). The European VLBI Network (EVN) is a joint facility of independent European, African,
517 Asian, and North American radio astronomy institutes. *e*-MERLIN is a National Facility operated by the
518 University of Manchester at Jodrell Bank Observatory on behalf of STFC. The National Radio Astronomy
519 Observatory is a facility of the National Science Foundation operated under cooperative agreement by As-
520 sociated Universities, Inc. This work has made use of data from the European Space Agency (ESA) mission
521 *Gaia* (<https://www.cosmos.esa.int/gaia>), processed by the *Gaia* Data Processing and Analysis
522 Consortium (DPAC, <https://www.cosmos.esa.int/web/gaia/dpac/consortium>). Fund-
523 ing for the DPAC has been provided by national institutions, in particular the institutions participating in the
524 *Gaia* Multilateral Agreement. Scientific results from data presented in this publication are derived from the
525 EVN project EY037 and the VLBA project BY145. The VLBI data processing and MCMC simulation in
526 this work made use of the compute resource of the China SKA Regional Centre prototype, funded by the
527 Ministry of Science and Technology of China and the Chinese Academy of Sciences.

528 **Author Contribution** X.-L.Y. designed the VLBI observations, made the VLBI data reduction and model-
529 fitting, interpreted the results, and drafted the manuscript. J.Y. double-checked the results by manual data
530 reduction. S.Y. and X.-L.Y. contribute to writing the VLBA observing proposal, A.-L.W., X.-L.Y., and T.A.
531 contribute to writing the EVN plus *e*-MERLIN observing proposal. All the authors discussed the results and
532 commented on the manuscript.

533 **Competing Interests** The authors declare that they have no competing financial interests.

534 **Correspondence** Correspondence and requests for materials should be addressed to X.-L. Y. (email:
535 yangxl@shao.ac.cn).

Table 1: **Model-fitting results of the radio components detected in IZw 1 with the VLBA L-band and EVN+e-MERLIN C-band observations.** Column 1: component name; Column 2: frequency; Column 3: right ascension offset, the uncertainty is 0.47 and 0.12 mas for 1.548 and 4.926 GHz, respectively; Column 4: declination offset, the uncertainty is 1.14 and 0.31 mas for 1.548 and 4.926 GHz, respectively; Column 5: integrated flux density; Column 6: angular size of components (if given) from a Gaussian model-fit; Column 7: lower limit of the radio brightness temperature.

Component	ν (GHz)	R.A.Off (mas, J2000)	DEC.Off (mas, J2000)	S_i (μ Jy)	Size (mas)	Log T_b (K)
(1)	(2)	(3)	(4)	(5)	(6)	(7)
W	1.548	-1.08	-0.95	348.75 \pm 3.48	0.07	10.57
E1	1.548	7.31	-1.43	480.93 \pm 4.80		6.85
E2	1.548	10.86	-2.05	754.82 \pm 7.54	4.81	7.63
E3	1.548	17.03	-4.73	426.85 \pm 4.26	4.24	7.34
E4	1.548	23.62	-0.78	173.03 \pm 1.73	1.01	7.96
N	1.548	9.58	8.90	150.84 \pm 1.50		6.34
S	1.548	-0.54	-15.25	168.46 \pm 1.68	27.51	6.16
Wb	4.926	-1.05	1.60	76.95 \pm 0.76	0.83	7.15
Wa	4.926	-2.09	2.28	65.95 \pm 0.65	0.001	12.39
W2	4.926	-14.14	6.42	34.67 \pm 0.34	0.47	7.22
E1	4.926	7.52	-1.23	91.07 \pm 0.91		6.29
E2	4.926	10.05	-1.06	107.72 \pm 1.07	6.46	5.97
E3a	4.926	13.68	-3.49	57.91 \pm 0.57		6.09
E3b	4.926	17.60	-4.68	31.97 \pm 0.32	1.39	6.33
N	4.926	9.89	3.01	69.59 \pm 0.69		6.17
S	4.926	-1.83	-2.91	53.14 \pm 0.53	0.73	6.98
X	4.926	6.22	-3.40	53.15 \pm 0.53		6.05

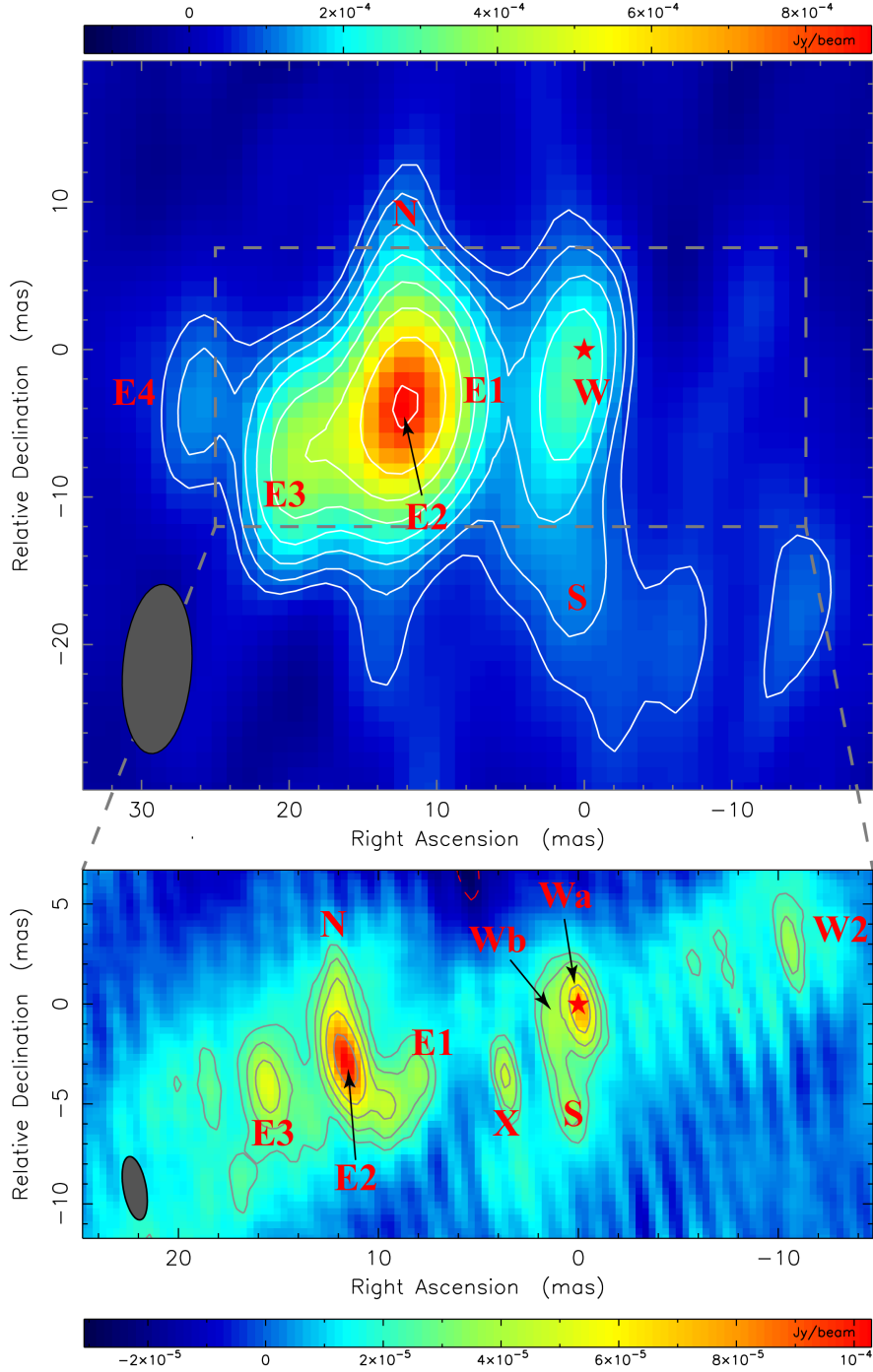


Figure 1: VLBI images of the IZw 1 in 1.54 and 4.92 GHz. The upper panel shows the cleaned L-band image and the lower panel shows the cleaned C-band image. In the L-band image, the beam size is 11.5×4.67 mas and the rms noise is 0.025 mJy/beam. In the C-band image, the beam size is 3.22×1.14 mas and the rms noise is 0.007 mJy/beam. At both images, the red asterisks indicate the *Gaia* position, the uncertainty of the *Gaia* position is $\Delta\alpha = 0.18$ and $\Delta\phi = 0.17$ mas at R.A. and DEC., respectively, including an astrometric excess noise error of 0.14 mas. All the images are produced with a natural weighting and the map reference is at the *Gaia* position, the contours are at $3\sigma \times (-1, 1, 1.41, 2, 2.83, \dots)$. At the redshift of IZw 1, 1 mas corresponding to 1.139 pc. The components are recognised based on the delta-model-fitted images except for the component X, which we cannot match with the model-fitted image.

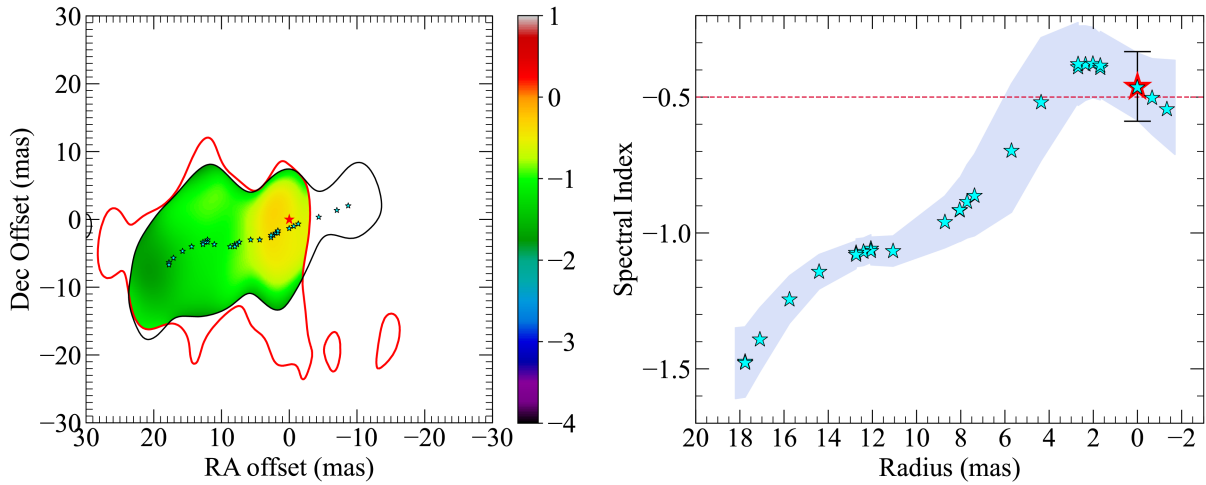


Figure 2: **1.5–5 GHz spectral index distribution of I Zw 1 on the parsec scale.** Left panel: the image was produced by using the naturally weighted clean map at 1.54 and 4.92 GHz. The region with radio flux density below 3σ was set as blank (white), i.e. the outer region of the red and white lines, respectively. Radio spectral indexes within both red and black lines are most reliable. The cyan asterisks indicate the jet ridgeline obtained from the tapered 4.92 GHz image; Right panel: the spectral index distribution along the ridgeline, the positive radius corresponding to the positive right ascension coordinates, and vice versa, and the *Gaia* position is set as the reference. The blue belt is the uncertainty of spectral index, in both panels the red asterisk indicates the *Gaia* position.

536 1 Supplementary

537 **The jet wiggling** The jets at both 1.5 and 5 GHz is strongly nonlinear, with a position angle cov-
538 erage of 18° at the approaching jet (the east branches). The non-linearity grows with the distance
539 from the core and the jet wiggling is more likely periodic than random (Figure 7), hints a helical
540 jet structure. We use the components from δ -model fitting of the tapered 5 GHz image to depict
541 the ridgeline of the jet limb (see Methods), and the ridgeline clearly shows a helical pattern. In the
542 5 GHz image (Figure 4), we also found the counter jet, which is more clear in the tapered image
543 (Figure 4), indicating the two-sided jet. Under the assumption of symmetrically approaching and
544 receding jets, we can estimate the inclination angle i to the line of sight and the jet velocity β
545 ($\beta = v/c$, where v is velocity, c is the speed of light, see Methods). Figure 6 shows the radio flux
546 density versus distance from the core. The radio emission at ~ 1 and ~ 10 mas region may be due
547 to additional Doppler boosting of the helical jet and/or collisions with the surrounding medium,
548 therefore which was not used for fitting. Based on the data, we give $\beta \cos i \sim 0.050 \pm 0.002$. This
549 model suggests a deceleration of the expanding jet plasma (expansion factor $\eta = 0.22 \pm 0.02$,
550 $\eta = 1$ for a linear expansion, see more details in Methods), consistent with a dense environment.

551 Employing the equation between the jet velocity and the inclination angle, we can fit the
552 geometric parameters of the helical jet structure. The helical model allows a good representation
553 of the jet structure, and in the MCMC fitting we can determine the parameters such as the jet
554 inclination angle to the line of sight $i = 87.6_{-1.1}^{+0.5}$ (deg), opening angle of helical jet cone $\psi =$
555 $5.7_{-1.1}^{+1.1}$ (deg), jet position angle with respect to the north on the sky plane anti-clockwisely $\chi =$
556 $101.4_{-0.5}^{+0.5}$ (deg), rotation period of jet position angle $P = 41_{-15}^{+27}$ (year) and jet velocity $v = 0.70 -$
557 1 (c). Note that the jet velocity is estimated by using the estimated value of inclination angle i and
558 the relation $\beta \cos i \sim 0.050 \pm 0.002$, the jet velocity is higher than the ultra-fast wind speed ($0.26 c$)
559 in IZw 1.

560 The helical jet structure in the super-Eddington accreting system IZw 1 enhances the simi-
561 larity between super-Eddington X-ray binaries such as SS 433 ³ and V404 Cygni ⁵, and with three
562 sources so far showing helical jets at super-Eddington accretions, we are almost coming to a con-
563 sensus and a strong demand for a unified model. The most plausible mechanism in driving the
564 helical jet structures is accretion disk precession. If the axis of the accretion disc is tilted to the
565 black hole spin, the frame-dragging generated by the black hole rotating can lead to particle pre-
566 cessing inside the disc, a.k.a. the Lense-Thirring effect ⁶⁰. The frame-dragging effect decreases
567 with distance and becomes negligible at large distances. Therefore an inclined viscous accretion
568 disk with respect to the spin of the black hole will produce warps in the disk which force the align-
569 ment between the axis of the innermost accretion disk and spin of the black hole, this phenomenon
570 is known as the Bardeen-Petterson effect ⁶¹. Our observations of IZw 1 demonstrate kpc-scale
571 molecular disk (direction of the axis) is tilted with the inner accretion disk axis or BH spin (see
572 main text), both hint the Lense-Thirring effect is at work.

573 The preset disk tilt/warping can be driven by several mechanisms, for example, the tides from
574 a companion star ⁶² or a black hole ⁶³, winds ⁶⁴, magnetically driven outflows ⁶⁵ and radiation driven
575 warping instability, a.k.a. the Pringle's instabilities ⁶⁶. Interestingly, a high or super-Eddington
576 accretion is often coupled with the wind ¹⁸ and the Pringle's instabilities ⁶⁶, supporting the helical

577 jet in super-Eddington accreting systems. The period of Lense–Thirring precession $P \propto M/a_*$
578 satisfies the scaling relation of black hole mass M , where a_* is the dimensionless black hole spin.
579 By comparison, we have calculated the value Pa_*/M , where P is in *min* and M is in M_\odot , which
580 is ~ 0.07 – ~ 0.09 and $\sim 1.35a_*$ – $\sim 3.84a_*$ for V404 Cygni ⁵ and IZw 1, respectively, the
581 spin parameter of IZw 1 is unknown. If considering the low and intermediate spin parameters
582 ($a_* \sim 0.1$ ⁶⁷), the helical jet structure in IZw 1 is consistent with the Lense–Thirring precession in
583 V404 Cygni.

584 **Large-scale radio emission** Figure 10 shows IZw 1 has a power-law radio spectrum over the
585 entire observed frequency range, indicating the dominance of synchrotron radiation, which does
586 not significantly affect by the collection areas, see Figure 11, where the intercept between the L-
587 band and C-band lines is the spectral index. The overall spectral index is -0.88 ± 0.10 , there is no
588 significant decrease at higher frequencies, indicating a continuous replenishment of fresh electrons
589 ⁶⁸, while the central engine remains active. Interestingly, the spectral index at the farthest edge of
590 the jet from the core is ~ -1.8 (Figure 2), which are inconsistent with the overall spectral index
591 estimated for the larger area but suggesting a non-jet origin as the spectral index decreases along
592 the jet direction. The large-scale flux density is dominated by diffuse radio emission with only a
593 fraction ($\sim 30\%$ out of 60 kilo-parsec scale and $\sim 47\%$ out of ~ 1.54 kilo-parsec scale emission
594 in 1.5 GHz) coming from the (parsec-scale) core region. The distribution of radio flux density can
595 be fitted as $S_L = (1.40 \pm 0.16)r^{0.165 \pm 0.010}$ and $S_C = (0.86 \pm 0.01)r^{0.137 \pm 0.002}$, where S_L and S_C is
596 the L and C-band flux density in mJy, and r is the angular size in mas (Figure 11).

597 Both star-forming activities and relativistic winds can produce large-scale radio emission ¹³,
598 here the star-forming activities are preferentially referred to supernovae or supernova remnants due
599 to the power-law spectrum. Assuming the whole radio emission is from the star-forming activities,
600 we can estimate the star formation rate (SFR) with radio emission by using the SFR-radio relation
601 (formula 3 in refs. ¹²). The largest SFR can be obtained with the datasets: NVSS at 1.4 GHz,
602 AE0022 at 1.4 GHz and 4.86 GHz, AA0048 at 14.94 GHz, which is $\sim 20 M_\odot \text{yr}^{-1}$, similar with
603 the estimate in (refs. ⁶⁹, $\sim 26 M_\odot \text{yr}^{-1}$), suggesting the large scale radio emission can be fully from
604 star-forming activities. Whereas the SFR-radio relation is quite crude that we can not fully rule
605 out the contribution of wind-like outflow, the radio-emitting wind at a large scale (a few kiloparsec
606 scale) is negligible. In addition, the radio-emitting wind is still possible at the intermediate scale
607 (tens of parsec scale), as there are no compact supernovae and supernova remnants detected by
608 VLBI and *e*-MERLIN observations ⁷⁰.

Table 2: **Summary of historical observations and results for IZw 1.** Column 1: telescope; Column 2: frequency; Column 3: project ID and references for datasets publication (NG: Not given; *: Original data is not available, the result is from literature); Column 4: observing date; Column 5: time-on-source; Column 6: observing bandwidth; Column 7 - 9: beam major axis, minor axis, and position angle; Column 10: integrated flux density; Column 11: peak flux density.

Telescope	ν (GHz)	Obs. ID	Date	TOS (min)	BW (MHz)	θ_{maj} (arcsec)	θ_{min} (arcsec)	P.A. (degree)	S_i (mJy)	S_p (mJy beam ⁻¹)
(1)	(2)	(3)	(4)	(5)	(6)	(7)	(8)	(9)	(10)	(11)
VLA-D	1.49	AE0022 ⁷¹	1983-07-04	2.7	100	52.7	44.8	-14.9	8.40 ± 1.43	8.40 ± 1.62
VLA-D	1.40	NVSS*, ⁷²	1993-11-15	0.4	50	46	46	0	8.80 ± 0.13	7.61 ± 0.11
VLA-D	1.40	AV0226	1996-09-17	238	6.2	59.2	53.4	25.0	8.43 ± 0.30	8.37 ± 0.32
VLA-D	1.40	AV0226	1996-09-28	237.5	6.2	59.6	53.5	22.5	8.25 ± 0.34	8.27 ± 0.38
VLA-C	1.49	AB0417 ^{73,74}	1986-11-08	9.5	100	18.9	14.9	-35.1	6.68 ± 0.38	6.12 ± 0.43
VLA-C	1.34	AL0417	1997-07-18	190.8	12.5	10.2	8.83	5.19	6.45 ± 0.40	6.51 ± 0.45
VLA-C	1.35	AL0417	1997-07-24	195	12.5	11.1	8.34	-33.2	6.49 ± 0.40	6.17 ± 0.45
VLA-B	1.49	AG0173	1985-04-22	85	100	5.94	4.69	52.4	5.13 ± 0.33	4.19 ± 0.37
VLA-B	1.40	FIRST*, ⁷⁵	2011-03-26	1	256	4.3	4.3	0	5.30 ± 0.24	5.05 ± 0.27
VLA-A	1.42	AL0502	1999-08-26	5.5	100	1.36	1.27	10.9	5.18 ± 0.32	6.77 ± 0.36
VLA-A	1.42	AK0406	1995-07-20	6.1	100	1.68	1.41	-0.62	5.17 ± 0.26	4.89 ± 0.29
VLA-A	1.42	AC0624	2002-05-02	10.5	100	1.66	1.36	-5.28	5.28 ± 0.18	4.90 ± 0.20
Arecibo	2.38	NG*, ⁷⁶	1975-08-01		16	162	162	0	4.00 ± 4.00	
VLA-BnA	2.98	VLASS1.1*, ⁷⁷	2017-10-08	0.1	2048	3.06	2.28	52.7	3.71 ± 0.25	2.86 ± 0.11
VLA-BnA	2.98	VLASS2.1*, ⁷⁷	2020-07-16	0.1	2048	2.68	2.37	36.6	3.63 ± 0.38	2.72 ± 0.18
VLA-D	4.86	AE0022	1983-07-04	12.7	100	12.9	11.1	-10.5	3.16 ± 0.25	2.27 ± 0.29
VLA-C	4.89	AK0298	1992-05-18	27.5	100	9.83	4.90	55.9	2.80 ± 0.07	1.34 ± 0.07
VLA-C	4.89	AB0417 ^{73,74}	1986-11-08	9	100	5.56	4.72	-33.9	2.46 ± 0.11	2.47 ± 0.13
VLA-B	4.86	AL0454	1998-09-02	8.6	100	1.51	1.38	7.61	2.20 ± 0.08	2.13 ± 0.09
VLA-A	4.89	AK0096 ⁷⁸	1983-11-23	25.1	100	0.50	0.42	-29.1	1.85 ± 0.08	1.79 ± 0.09
VLA-A	4.86	AK0406	1995-07-20	9.5	100	0.49	0.41	-2.14	2.18 ± 0.10	2.02 ± 0.11
VLA-A	4.86	AC0624	2002-05-02	9.8	100	0.48	0.41	11.6	1.85 ± 0.08	1.85 ± 0.09
MERLIN	4.99	96DECA	1996-12-01	558	15	0.08	0.05	22.35	1.46 ± 0.15	1.43 ± 0.18
MERLIN	4.99	97NOVC	1997-11-06	450	15	0.08	0.04	20.04	1.51 ± 0.42	1.83 ± 0.48
VLA-B	8.46	AC0624	2002-08-09	9.8	100	0.68	0.65	20.2	1.46 ± 0.11	1.15 ± 0.13
VLA-A	8.43	AP0212	1991-06-24	14.8	100	0.26	0.24	59.7	0.94 ± 0.14	0.90 ± 0.08
VLA-A	8.46	AB0670	1992-12-04	119.3	100	0.27	0.26	-12.2	1.18 ± 0.02	1.09 ± 0.02
VLA-C	14.94	AA0048 ^{73,74}	1985-07-28	14.5	100	1.87	1.49	-29.5	1.20 ± 0.38	1.20 ± 0.43
OVRO-40	20.00	NG*, ⁷¹	1983-07-07		400	90	90	0	< 1.90	< 1.90
VLA-C	22.46	AA0048 ^{73,74}	1985-07-28	29	100	1.13	1.01	-48.9	< 1.91	< 1.91
VLA-A	22.46	AP0210	1991-07-02	18.5	100	0.38	0.09	-56.8	< 1.76	< 1.76

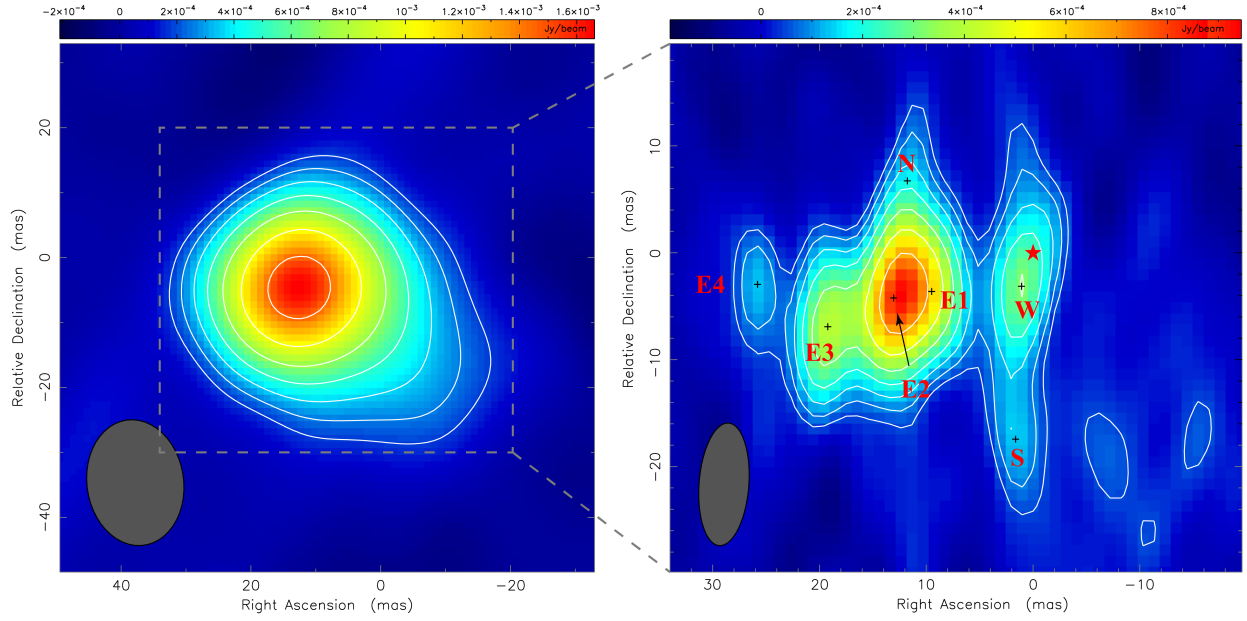


Figure 3: **Radio images of the I Zw 1 in 1.54 GHz obtained with VLBA observation.** The left panel shows the tapered image with a beam size of 19.9×14.9 mas, the rms noise is 0.06 mJy/beam. The right panel shows the delta-model-fitted image with a beam size of 11.5×4.67 mas and the rms noise is 0.029 mJy/beam. In the delta-model-fitted image, the black crosses show the location of components, the red asterisks indicate the *Gaia* position, the uncertainty of the *Gaia* position is $\Delta\alpha = 0.18$ and $\Delta\delta = 0.17$ mas at R.A. and DEC., respectively, including an astrometric excess noise error of 0.14 mas. All the images are produced with a natural weighting and the map reference is at the *Gaia* position, the contours are at $3\sigma \times (-1, 1, 1.41, 2, 2.83, \dots)$. At the redshift of I Zw 1, 1 mas corresponding to 1.139 pc.

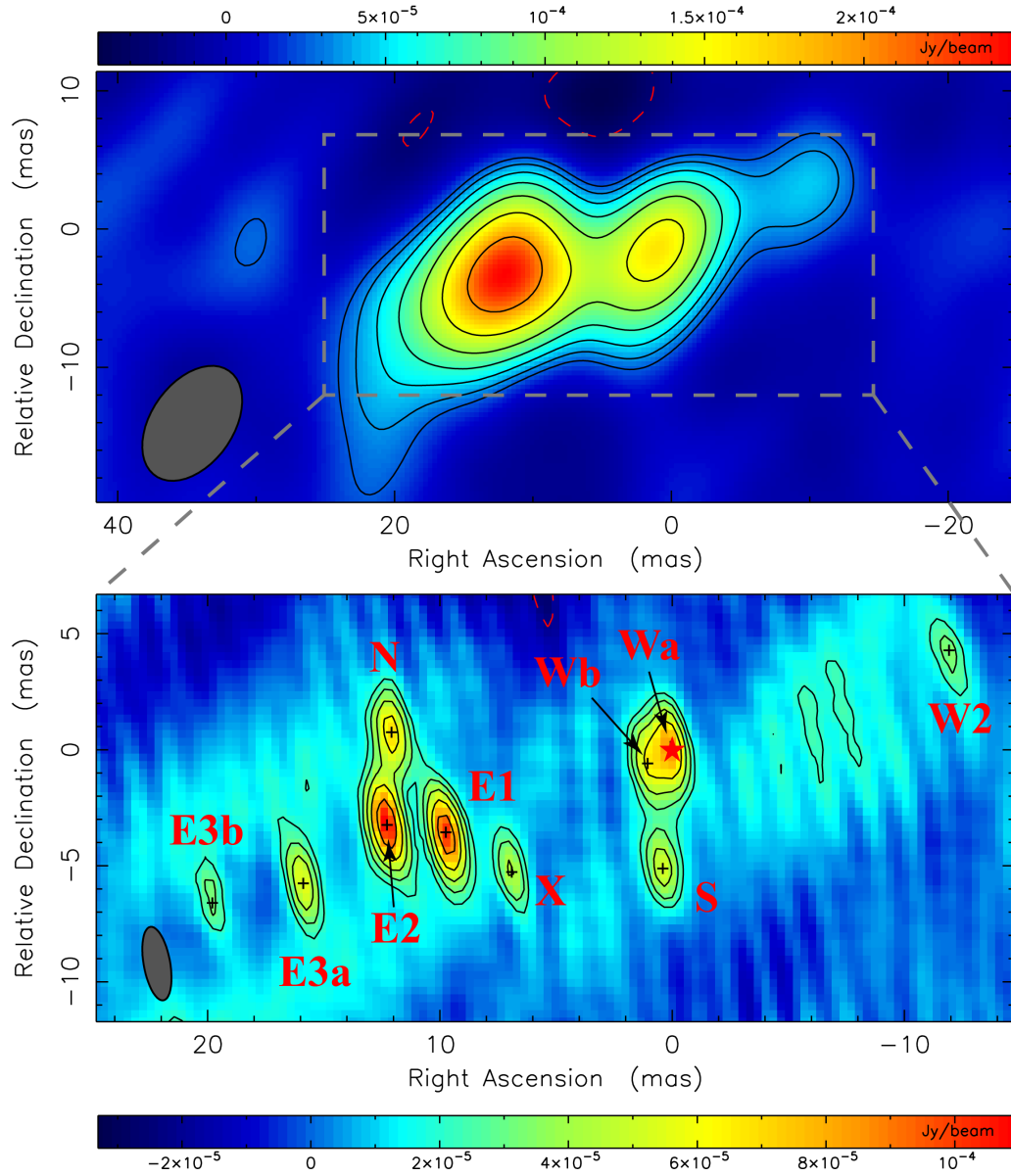


Figure 4: **Radio images of the I Zw 1 in 4.92 GHz obtained with EVN plus *e*-MERLIN observation.** The upper panel shows the tapered image with a beam size of 9.27×5.95 mas, the rms noise is 0.01 mJy/beam. The lower panel shows the delta-model-fitted image with the beam size of 3.22×1.14 mas and the rms noise of 0.007 mJy/beam, the blue crosses show the location of components, the red asterisks indicate the *Gaia* position. The delta-model-fitted image only shows the most compact components, the component E3a and E3b is revealed at the delta-model-fitted image and the component X can not be recognised as it's not matched between the cleaned and model-fitted images. All the images are produced with a natural weighting and taking the *Gaia* position as the reference point, the contours are at $3\sigma \times (-1, 1, 1.41, 2, 2.83, \dots)$.

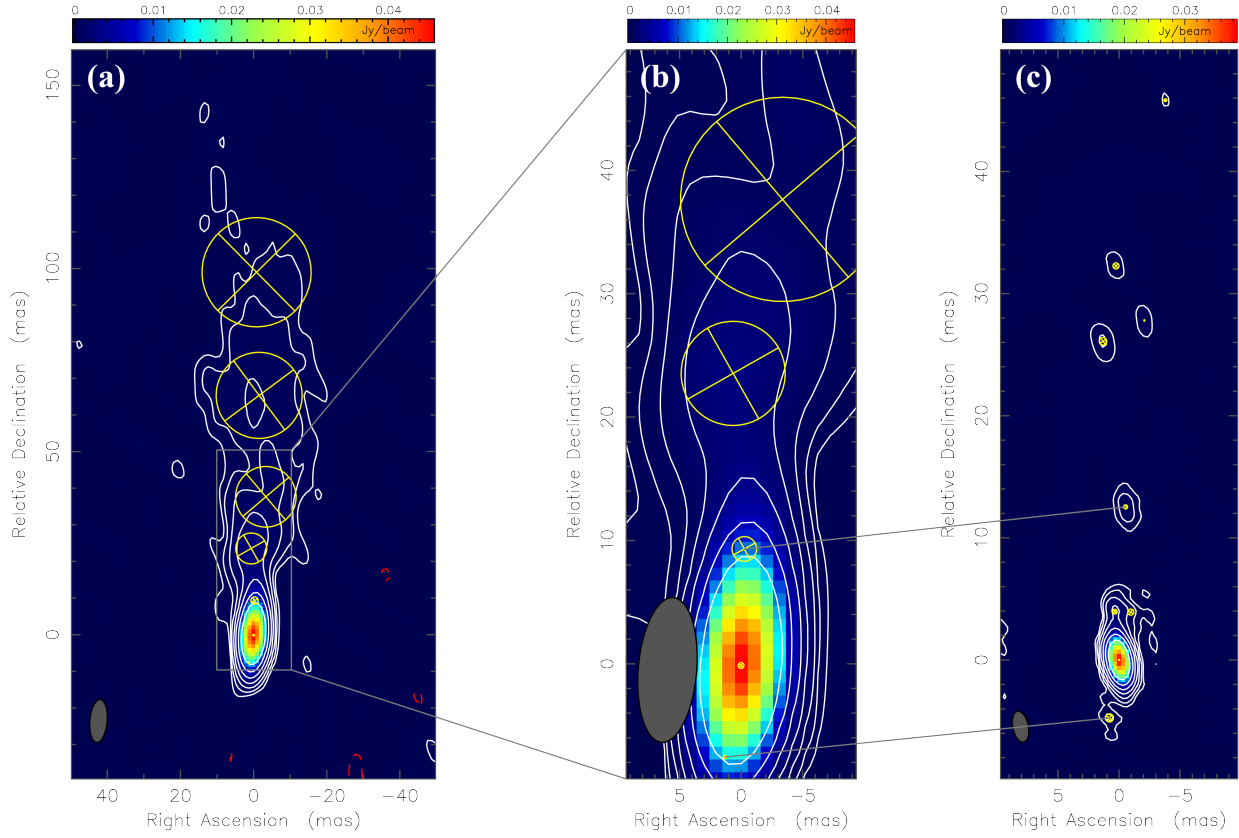


Figure 5: **Model-fitting images of the phase calibrator J0056+1341 at 1.54 GHz (panel a and b) and 4.92 GHz (panel c).** The images are produced using two-dimensional Gaussian model fitting with natural weights, with contours plotted as $3\sigma \times (-1, 1, 2, 4, 8, \dots)$, where σ is the root mean square (rms) noise. The black solid lines represent positive values and the red dashed lines represent negative values. The rms noise is 0.2 mJy/beam for both 1.54 and 4.92 GHz images. The model-fitting components are superimposed as yellow circles. The grey ellipses at the bottom left corner of each panel represent the full-width at half-maximum (FWHM) of the restoring beam. The grey lines between panels c and b indicate the corresponding components without the core-shift effect, i.e. the optically thin components.

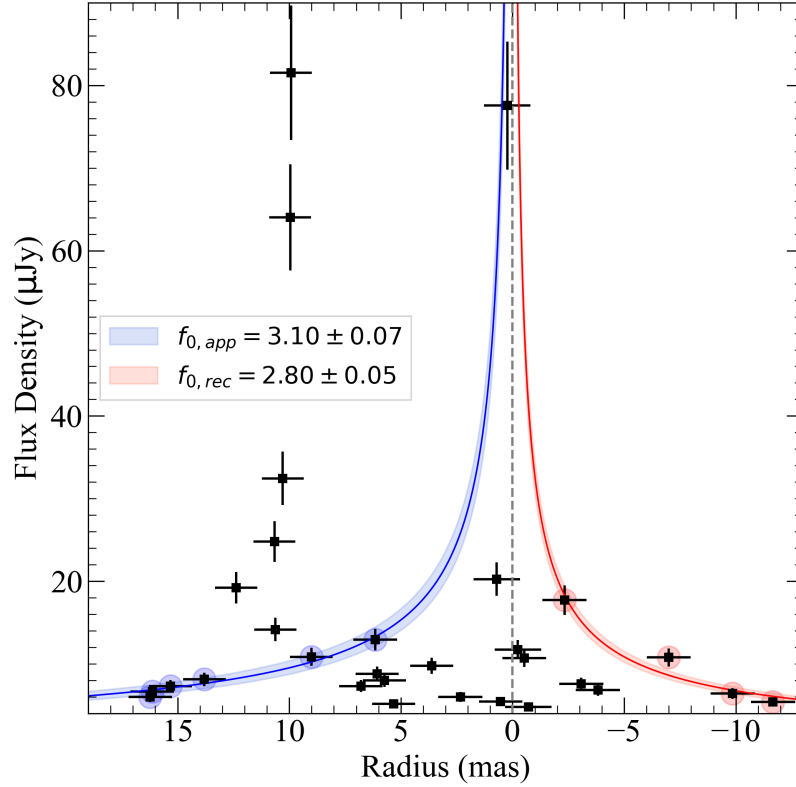


Figure 6: **Constraints on the flux density factor b and expansion factor η with the adiabatic jet expansion model for I Zw 1.** The model is constrained on the radio flux density distribution along with the distance to the core, where the data points with positive and negative radius are the approaching and receding jet, respectively. The radio flux density is from clean components at 4.92 GHz, where only the bright components (marked with the blue and red circle) are used for least-square fitting, the components at radius ~ 1 and ~ 10 mas are not considered in the fitting. The blue and red solid line indicates best-fit results for approaching and receding jets, respectively, where the blue and red belt is the 1σ error.

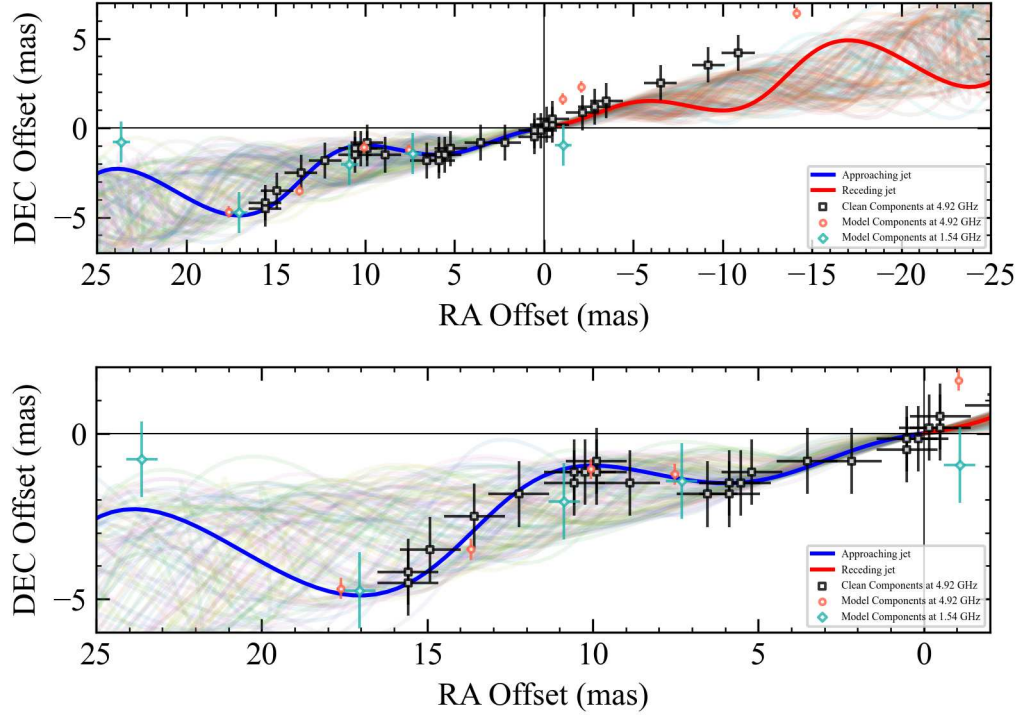


Figure 7: **Jet (blue) and counter jet (red) based on the parameters of maximum likelihood and random sampling.** The blue and red solid lines based on the parameters: inclination angle $i = 87.6^\circ$, opening angle of jet precessing cone $\psi = 5.7^\circ$, position angle to the north anti-clockwise $\chi = 101.4^\circ$, angular velocity $\Omega = 8.59 \text{ deg/year}$ and angle of terminal jet components with respect to the line of sight $\theta = -136^\circ$.

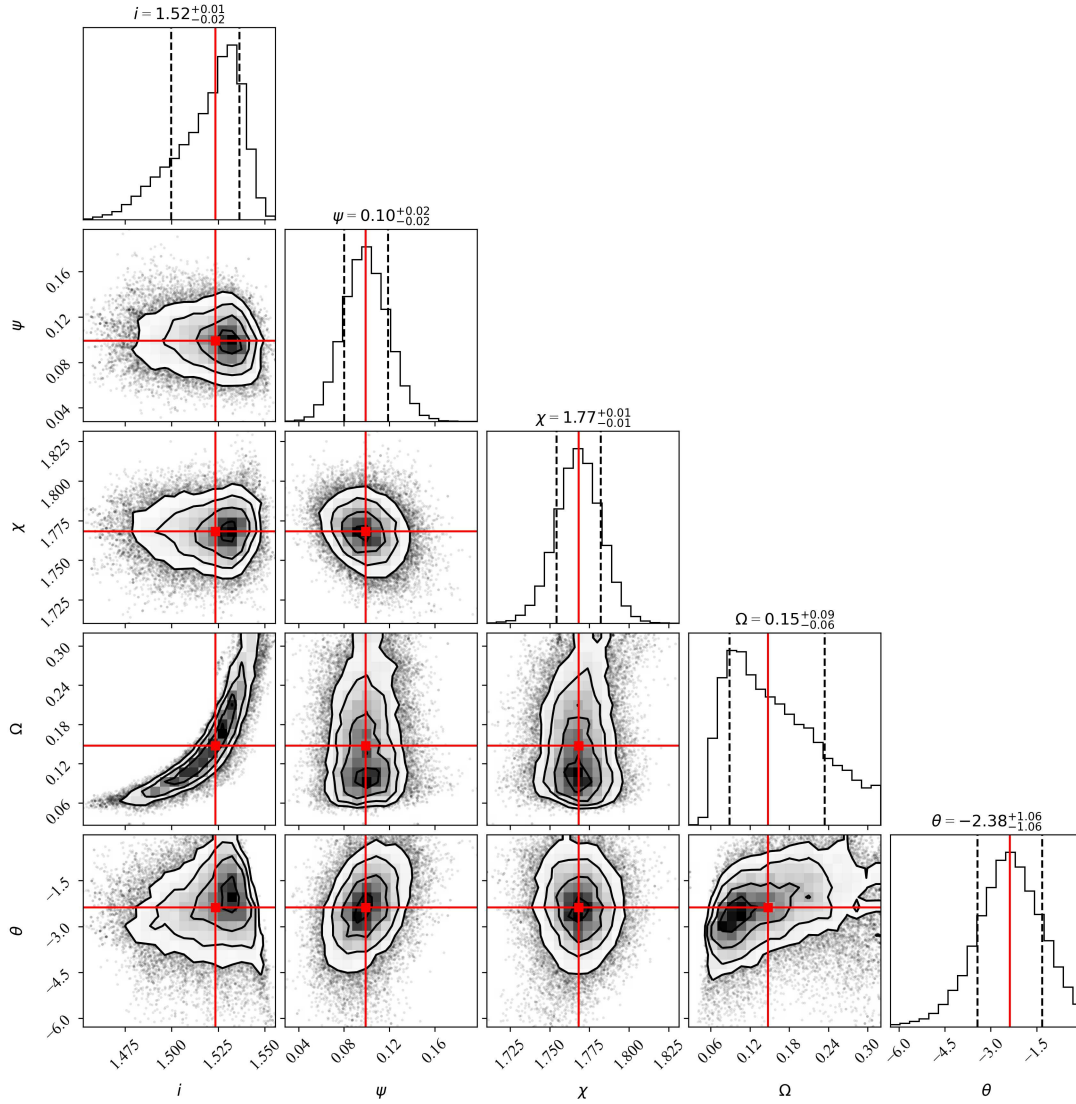


Figure 8: **Marginalised and joint posterior probability distribution for the model parameters in the mcmc approach.** We only show four parameters: inclination angle i in radians, opening angle of jet precessing cone ψ in radians, position angle to the east χ in radians and precession period Ω in *radian/year*, additionally, the jet velocity was correlated with inclination angle i in equation 9. The cross lines marker the values from a least-square fitting.

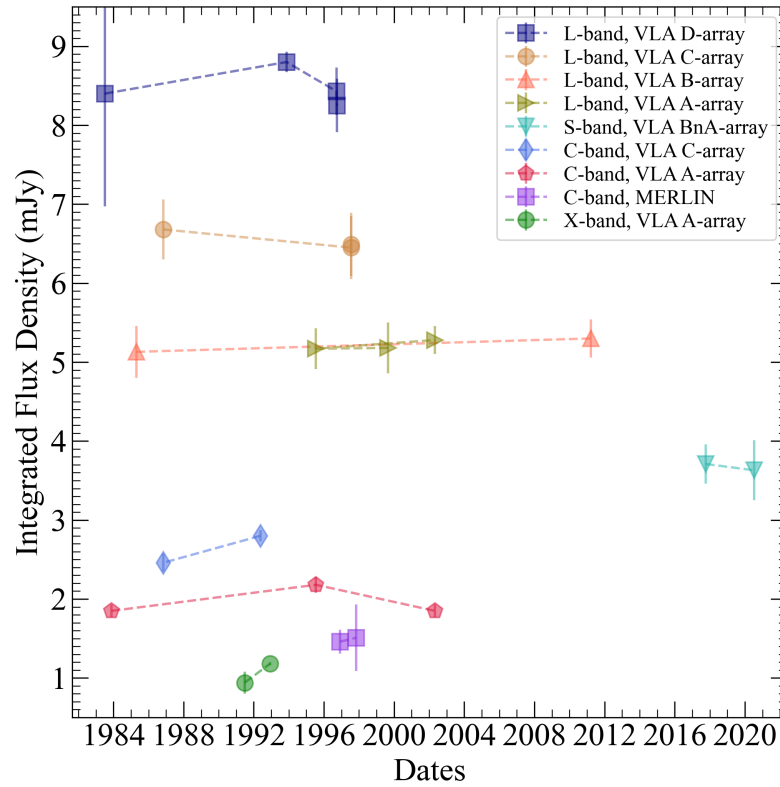


Figure 9: **The radio flux density of I Zw 18 over a time interval of 37 years.** The integrated radio flux densities and their uncertainties are taken from Table 2, where the data with the same observing band (approximately equal central frequencies) and arrays/sub-arrays are concatenated to show the variability.

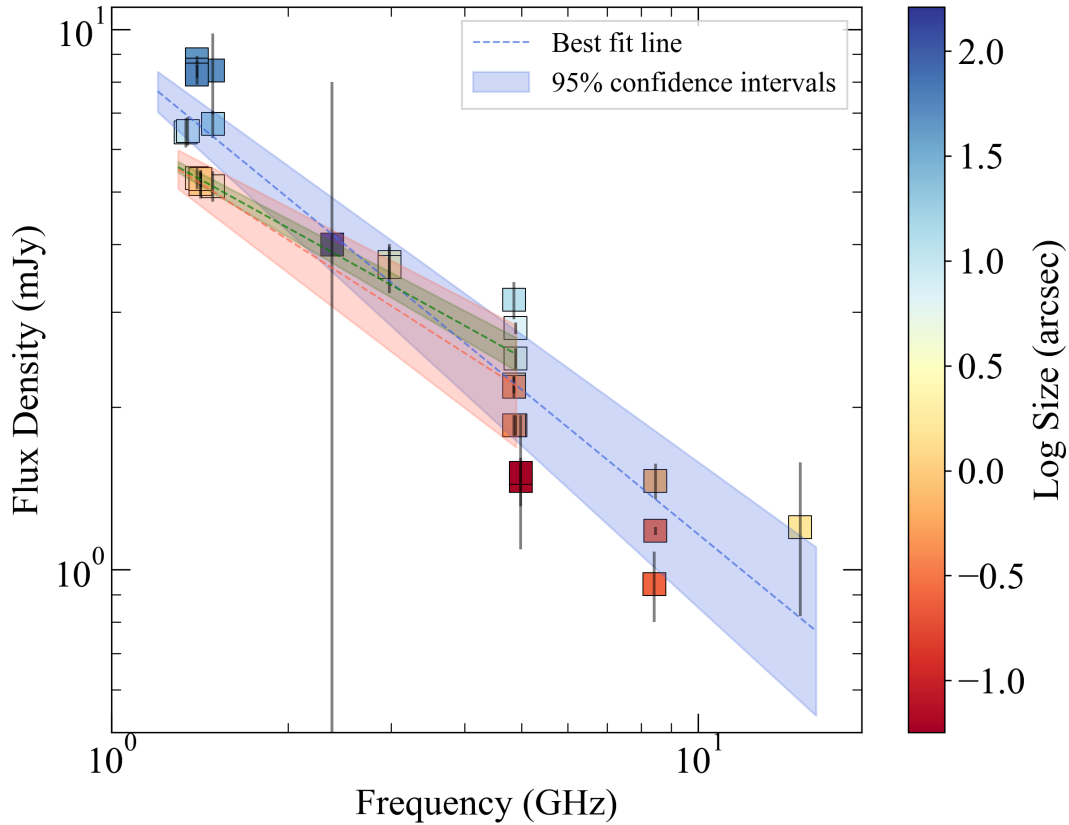


Figure 10: **Wide-band radio spectrum of IZw 1.** The integrated radio flux density measurements of IZw 1 in five radio frequency bands between 1.4 and 15 GHz are shown, where the flux density and uncertainties are taken from Table 2. The blue dashed line is the model-fitting result with a power-law spectrum using all the data points presented here. The power-law slope (spectral index) is -0.88 , the blue belt shows the 95% confidence intervals (0.10). The green and red dashed lines show the power-law fitting between 1.4 and 5 GHz datasets with similar size scales, i.e. 1.3~1.5 (red) and 4.3~5.3 (green), respectively, the green and red belts indicate their 95% confidence intervals, respectively.

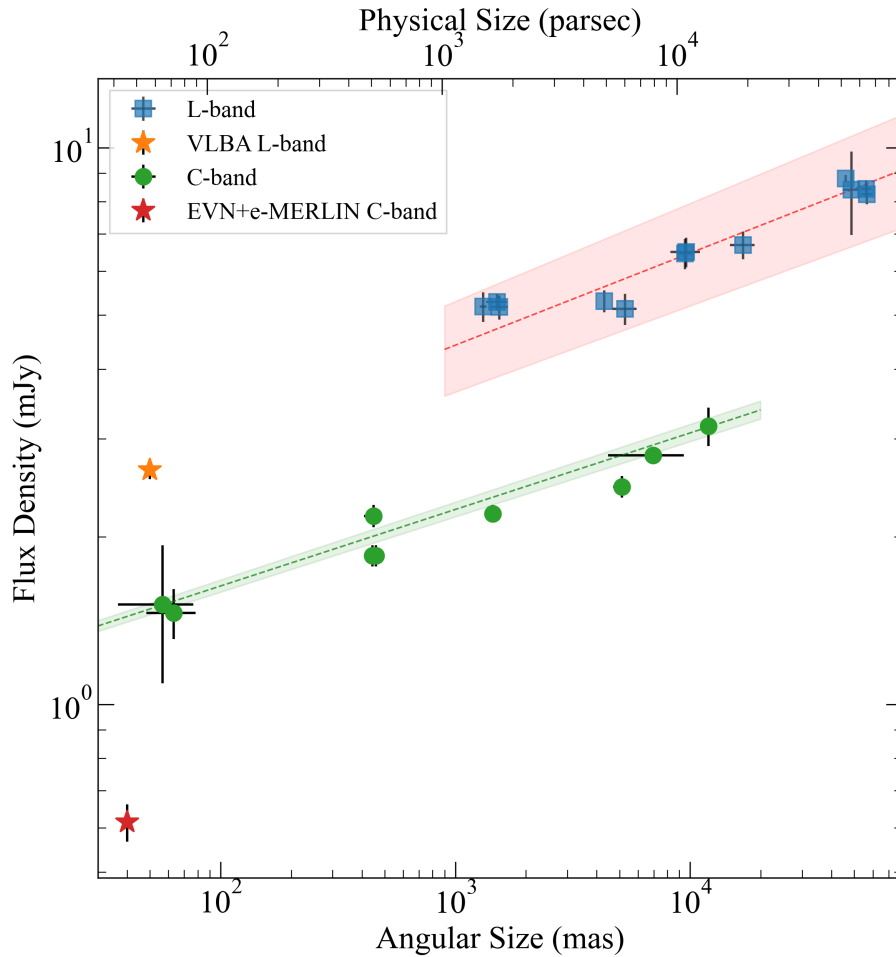


Figure 11: **The radio flux density of IZw 1 over a collection area range from ~ 0.04 to ~ 50 arcsec.** The integrated radio flux densities and uncertainties of IZw 1 in L and C bands are shown, which are taken from Table 2. As IZw 1 is not resolved in the given observations, the synthesised beams are taken to represent the collection area. The dashed lines and belts show power-law fittings and 95% confidence intervals, respectively, at L (red) and C-band (green). The intervals between L and C-band flux density represent the radio spectral index.